國立交通大學

電信工程研究所

碩 士 論 文

利用漸近邊界條件分析表面波於皺褶結構之色散

Surface Wave Dispersion Analysis of Planar Corrugated Surfaces by Asymptotic Corrugations Boundary Conditions

研 究 生：嚴大龍　　(Ta-Lung Yen)

指導教授：黃謀勤　博士　(Dr. Malcolm Ng Mou Kehn)

中 華 民 國 一 百 零 一 年 七 月

利用漸近邊界條件分析表面波於皺褶結構之色散

學生：嚴大龍　　指導教授：黃謀勤 博士

國立交通大學電信工程研究所碩士班

摘　　要

電磁能隙(Electromagnetic Bandgap, EBG)結構在近年來被廣泛的研究與應用，而皺褶性結構是其代表之一。在探討 EBG 結構時，色散圖(Dispersion diagram)和反射相位(Reflection phase)是兩個最重要的特性。在此篇論文中，我們將研究如何準確及快速地獲得皺褶性結構的色散圖，藉由近似法和邊界條件，從基本向量勢與電磁場的關係中推導出其特徵方程式，從方程式進而得到完整的色散圖。接著我們會與傳統獲取色散圖的方法: 橫向共振技術 (Transverse Resonance Technique, TRT)以及模擬軟體來做比較，藉此來評估其準確性及快速性。我們最後也實際建造了一個皺褶性結構，藉由散射參數來間接證明此特徵方程式所得的色散圖。

傳統上研究皺褶性結構時，會著重當波行進方向為在皺褶結構表面上 0 度或者 90 度時的情況，也就是所謂的軟和硬表面(Soft/Hard surfaces)。此篇論文會進一步探討波斜向入射時的情況。藉由觀察皺褶性結構的色散圖，我們將會發現其與一般週期性結構不一樣的地方，故我們亦會研究此特性對於不同方向的表面波在皺褶性結構上行進時會有何影響。

在量測階段時，通常無法直接獲取色散圖，而必須透過散射參數來間接說明，然而我們希望能夠透過量測還原出色散圖。因此在此篇論文，我們探討散射參數與波數之間的關係，期許可以將量測的散射參數有效地還原成色散圖。目前我們已經可以將模擬的散射參數數據還原成色散圖，期許將來可以應用在實際地量測數據。

Surface wave dispersion analysis of planar corrugated surfaces by asymptotic corrugations boundary conditions

Student：嚴大龍　　Advisor：Dr. Malcolm Ng Mou Kehn

Institute of Communications Engineering
National Chiao Tung University

ABSTRACT

Electromagnetic bandgap (EBG) structures had been widely investigated in literature in recent years, and the planar corrugated surface is one of them. In studying such structures, the dispersion and reflection phase diagrams are two of the most important characteristics. In this thesis, we will study how to retrieve the dispersion diagram of the corrugations accurately and rapidly. By an asymptotic method and the use of classical vector potentials, we can derive the characteristic equation, thereby obtaining the surface-wave dispersion diagram. To demonstrate its accuracy and quickness, the method we proposed will be compared to a full wave simulator and the transverse resonance technique (TRT), the latter being a traditional method for getting the dispersion diagram. Finally, we fabricated a corrugation, and measure its scattering parameters to indirectly verify the dispersion diagram obtained by the method we proposed.

In traditional studies of corrugations, surface-wave propagations along only the two principal directions are considered, pertaining to the so-called soft and hard surfaces. In this thesis, we will further explore the situation whereby the wave propagates obliquely on the surface. By observing the dispersion diagram of the corrugations, we will notice its difference compared to normal periodic structures, and then explain the wave propagation properties on the corrugation surface.

At the measurement stage, it is difficult to get the dispersion diagram directly, and usually the scattering parameters are used to explain the width and position

in the frequency spectrum of the bandgaps. In the thesis, the relationship of the scattering parameters and wavenumbers are discussed, so that the measured scattering parameters can be transformed to the dispersion diagram effectively. So far we succeed in transforming the simulated scattering parameters to the dispersion diagram, and we hope this method can be applied to measured data in the future.

誌謝

首先感謝我的指導教授 黃謀勤博士在我碩士生涯這兩年的指導與栽培，無論何時去他的辦公室請教問題，總是願意撥空來指導我，並且在研究上給予我專業的知識以及正確的方向。也謝謝他給予我機會讓我參加國外的會議論文研討，讓我見識到了來自各國學者精闢的報告，同時第一次以英文演說也是一個難忘的經驗。

另外，我也要感謝我實驗室的同學樞彥，由於我們是 黃謀勤博士第一屆的學生，在這兩年中樞彥幫忙處理了很多實驗室的事情，讓實驗室的運作漸漸步上軌道。同時在研究的過程，我們也常常彼此互相討論交流，在這過程讓我收穫良多。也謝謝光子晶體實驗室的正元、芳銚、和宜哲學長，在我研究遇到瓶頸或者軟體操作上有問題時，都能適時給予寶貴的意見與幫助。也謝謝實驗室的學弟妹:建融、博丞、怡嘉、以及 Lallah，你們的加入讓實驗室的氣氛更熱鬧、更有活力。

最後，我要謝謝我的家人，在這兩年來的支持與鼓勵，他們從不給我壓力，讓我每次回高雄時都覺得像充了一次電，回學校時更能專心在我的研究上，你們的疼愛與關懷使我備感溫馨。

TABLE OF CONTENTS

LIST OF FIGURES

I. Introduction

Corrugations have been an objective of keen interest in electromagnetic theory for many decades. Elliott was one of the earliest pioneers, who studied the surface wave propagation over a corrugated metallic ground plane, and has been concerned with the problem where the directions of wave propagation across the surface is normal to the corrugations [1]. Since the wave propagation direction will not always be normal to the corrugation, Hougardy and Hansen studied the surface wave propagation along an oblique angle with the orientation of the corrugations [2].

Theoreticians and computational enthusiasts were not the only ones captivated by this structure. Experimentalists and practical engineers have, likewise for the past many years, been making use of corrugations to develop improved microwave devices such as waveguides and antenna. The most known applications for corrugation are soft and hard surfaces, and the ideas were first introduced by Kildal [3] [4]. These surfaces triggered interests from enormous researchers because they can control the behavior of wave propagation over them. In other words, wave propagation can either be suppressed (soft) or enhanced (hard) on these surfaces, as shown in Fig.1. For examples, the soft surface is often called “chokes” and used to reduce the cross-polarization and sidelobes in particular directions. The hard surface is used to design hard horns which have high aperture efficiency or reduce scattering from masts that block the radiation field of an antenna [5].

The soft and hard surfaces have similar notions with the electromagnetic bandgap (EBG) structures, whereby both demonstrate the wave propagation existed in some frequency band and prohibited in others. In [6], the EBG structures are defined as artificial periodic objects that prevent/assist the propagation of electromagnetic waves in a specified band of frequency “for all incident angles” and all polarization states, while only for some specular angles for soft and hard surfaces. The EBG structures have become a popular topic in the antenna community since its useful application. The attracting features include designing an efficient low profile wire antenna near a ground plane [7], being applied for high gain resonator antennas [8], and for surface wave suppression [9]. Despite the numerous works on corrugated surfaces found in literature, none has studied them in terms of the dispersion diagram conveying the surface-wave passband and stop-band properties, or presented characteristic equations from which the aforementioned diagram is obtained. Field distributions of the surface wave modes supported by the corrugations are also nowhere to be found.

The main properties when investigating the periodic structures will be the dispersion diagram and reflection phase. In this thesis, we will focus on the points with the dispersion diagram of the corrugation. Due to the complexity of the EBG structures, it is usually difficult to characterize them by analytical methods. So we can utilize approximate boundary

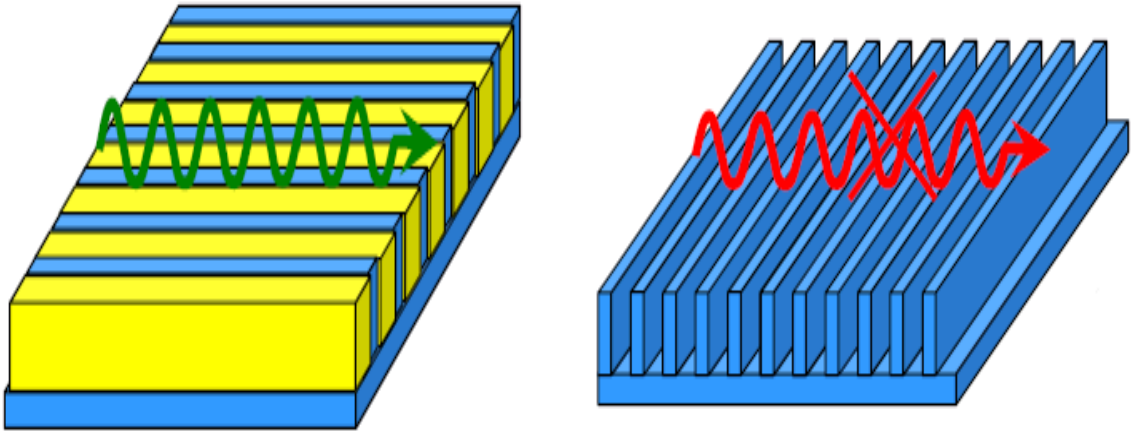

(a) (b)

Figure 1: (a) Hard (b) soft surfaces

conditions (ABC) to provide an approximate relationship between the electric and magnetic field on a chosen surface. The simplest case might be the first order impedance conditions, sometimes referred to as SIBC (Standard Impedance Boundary Conditions), which are applicable at the surface of a lossy dielectric. For some cases, the accuracy of SIBC is not sufficient, so generalized impedance boundary condition (GIBC) with more degrees of freedom is proposed to have higher accuracy. The works in [10] and [11] have used such approximate impedance boundary conditions to study corrugated surfaces. In fact, some approximations have been around for a long time, even though the classical condition E_{tan} =0 at the surface of a metal is regarded as exact, but actually it is also the approximation even at microwave frequencies.

In early periods, in order to analyze corrugated and strip-loaded surface accurately, the fields must be expanded to Floquet modes or parallel plate waveguides modes which are very difficult and complicated. In [12], Kildal presented asymptotic corrugation and strip-loaded boundary conditions (ACBC and ASBC) for analysis of corrugated and strip-loaded surfaces, respectively. In this thesis, ACBC is used to derive the characteristic equation and thus obtain the dispersion diagram of planar corrugated surfaces, which has not been studied in other literatures so far. After observing the dispersion diagram, the unique and special characteristic of the corrugation will be discussed.

So far in the literature, most of the studies for periodic structures were working on achieving entire bandgap capabilities, especially seeking for a wider bandgap, for example, the mushroom-like surface and its modified types [13][14], as shown in Figs 2. However, not all applications require the suppression of surface-wave propagation in all directions on the surface. In fact, there may potentially be numerous situations where such entire bandgap

behavior is actually not needed at all, and some may even require suppression along only some directions but permission in all others. In other words, surface-waves are suppressed in certain directions but prohibited in other directions. The corrugated surface is one object we found which can achieve this idea. The reason is that corrugations can simultaneously process different bandgaps with respect to the different angles of incident surface waves. The phenomenon may also occur in other periodic structures, but we will show later that corrugations can reach the best effect.

In the final section of this thesis, we will introduce the relationship between the scattering parameters and the wavenumbers. The original goal was to obtain the dispersion diagram, but when it comes to the measurement stage, unfortunately, it is impossible to measure the wavenumbers directly. So most of the time in the literature, the way to explain the width and position in the frequency spectrum of bandgaps is through the scattering parameters, which are reflection and transmission coefficient ($|S_{11}|$ and $|S_{21}|$). For structures that can be represented by equivalent circuits, it is possible to get the relationship between the scattering parameters and wavenumbers by the ABCD matrix. But for more complex structures, the computation may be too elaborate. In [14], a method was described to retrieve the complex permittivity and permeability. We shall herein employ it to the scattering parameters of the corrugated surface to construct the dispersion diagram, which is then verified with the one generated by the characteristic equation derived from ACBC.

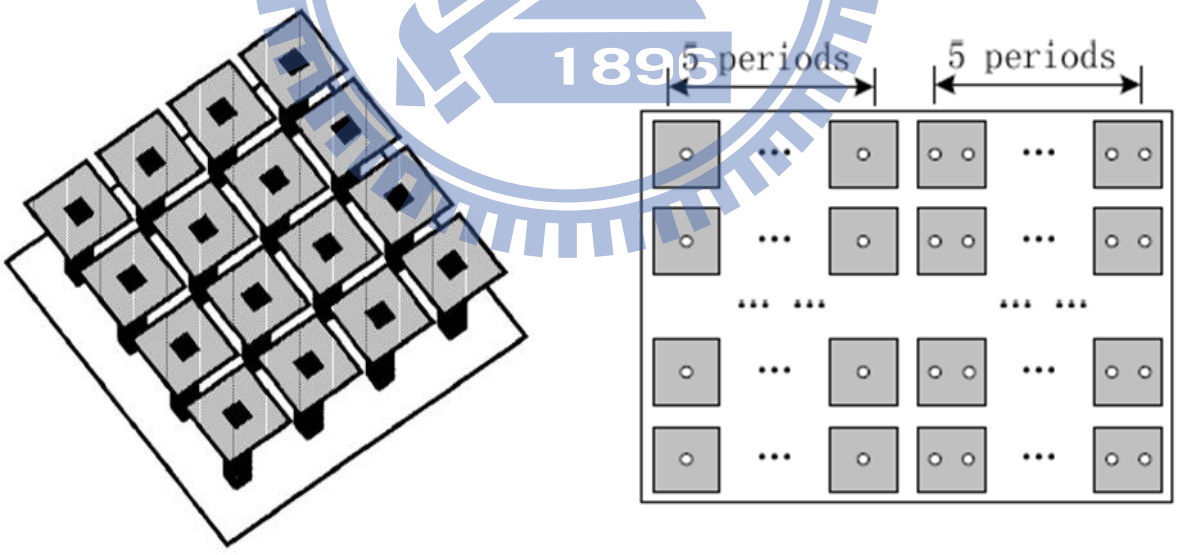

(a) (b)

Figure 2: (a) Mushroom-like EBG structures, (b) multi-via cascaded mushroom-like EBG structures.

II. Theory

2-1 Characteristic equation of the corrugation

The total **E** and **H** field are obtained by the superposition of the individual field due to **A** and **F**, where **A** and **F** represent the magnetic and electric vector potential, respectively.

$$E = E_A + E_F = [-j\omega A - j\frac{1}{\omega\mu\varepsilon}\nabla(\nabla\bullet A)] + (\frac{1}{\varepsilon}\nabla\times F) \tag{1}$$

$$H = H_A + H_F = (\frac{1}{\mu}\nabla\times A - j\omega F) + [-j\frac{1}{\omega\mu\varepsilon}\nabla(\nabla\bullet F)] \tag{2}$$

(1) and (2) can be expanded and be written as

$$\begin{aligned} E = {} & \hat{a}_x[-j\omega A_x - j\frac{1}{\omega\mu\varepsilon}(\frac{\partial^2 A_x}{\partial x^2}+\frac{\partial^2 A_y}{\partial x\partial y}+\frac{\partial^2 A_z}{\partial x\partial z}) - \frac{1}{\varepsilon}(\frac{\partial F_z}{\partial y}-\frac{\partial F_y}{\partial z})]\ldots \\ & \ldots+\hat{a}_y[-j\omega A_y - j\frac{1}{\omega\mu\varepsilon}(\frac{\partial^2 A_x}{\partial x\partial y}+\frac{\partial^2 A_y}{\partial y^2}+\frac{\partial^2 A_z}{\partial y\partial z}) - \frac{1}{\varepsilon}(\frac{\partial F_x}{\partial z}-\frac{\partial F_z}{\partial x})]\ldots \\ & \ldots+\hat{a}_z[-j\omega A_z - j\frac{1}{\omega\mu\varepsilon}(\frac{\partial^2 A_x}{\partial x\partial z}+\frac{\partial^2 A_y}{\partial y\partial z}+\frac{\partial^2 A_z}{\partial z^2}) - \frac{1}{\varepsilon}(\frac{\partial F_y}{\partial x}-\frac{\partial F_x}{\partial y})] \end{aligned} \tag{3a}$$

$$\begin{aligned} H = {} & \hat{a}_x[-j\omega F_x - j\frac{1}{\omega\mu\varepsilon}(\frac{\partial^2 F_x}{\partial x^2}+\frac{\partial^2 F_y}{\partial x\partial y}+\frac{\partial^2 F_z}{\partial x\partial z}) + \frac{1}{\mu}(\frac{\partial A_z}{\partial y}-\frac{\partial A_y}{\partial z})]\ldots \\ & \ldots+\hat{a}_y[-j\omega F_y - j\frac{1}{\omega\mu\varepsilon}(\frac{\partial^2 F_x}{\partial x\partial y}+\frac{\partial^2 F_y}{\partial y^2}+\frac{\partial^2 F_z}{\partial y\partial z}) + \frac{1}{\mu}(\frac{\partial A_x}{\partial z}-\frac{\partial A_z}{\partial x})]\ldots \\ & \ldots+\hat{a}_z[-j\omega F_z - j\frac{1}{\omega\mu\varepsilon}(\frac{\partial^2 F_x}{\partial x\partial z}+\frac{\partial^2 F_y}{\partial y\partial z}+\frac{\partial^2 F_z}{\partial z^2}) + \frac{1}{\mu}(\frac{\partial A_y}{\partial x}-\frac{\partial A_x}{\partial y})] \end{aligned} \tag{3b}$$

Since we want the field expressions that are independent of the coordinate system, for the transverse magnetic (TM) modes, it is acceptable to let the vector potential A have only a component, and the remaining components of A as well as all of F are set to be zero. To express the surface waves on the corrugation in Fig. 3, we derive the field expressions that are TM to y. Let

$$A = \hat{a}_y A_y(x,y,z) \tag{4a}$$

$$F = 0 \tag{4b}$$

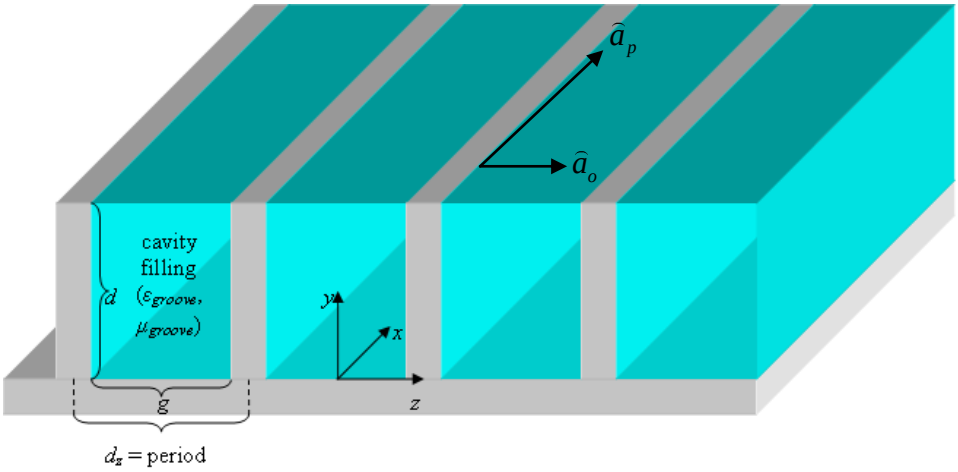

Figure 3: Infinite-long planar corrugated surface.

Then

$$E_x = -j\frac{1}{\omega\mu\varepsilon}\frac{\partial^2 A_y}{\partial x\partial y}, \qquad H_x = -\frac{1}{\mu}\frac{\partial A_y}{\partial z}$$

$$E_y = -j\frac{1}{\omega\mu\varepsilon}\left(\frac{\partial^2}{\partial y^2}+\beta^2\right)A_y, \qquad H_y = 0$$

$$E_z = -j\frac{1}{\omega\mu\varepsilon}\frac{\partial^2 A_y}{\partial y\partial z}, \qquad H_z = -\frac{1}{\mu}\frac{\partial A_y}{\partial x} \tag{5}$$

Similarly, we let the F vector potential have only a component in the y direction, and set the remaining components F and A as zero, then we can get the transverse electric (TE^y) modes. Let

$$A = 0 \tag{6a}$$

$$F = \hat{a}_z F_z(x,y,z) \tag{6b}$$

Then

$$E_x = \frac{1}{\varepsilon}\frac{\partial F_y}{\partial z}, \qquad H_x = -j\frac{1}{\omega\mu\varepsilon}\frac{\partial^2 F_y}{\partial x\partial y}$$

$$E_y = 0, \qquad H_y = -j\frac{1}{\omega\mu\varepsilon}\left(\frac{\partial^2}{\partial y^2}+\beta^2\right)F_y$$

$$E_z = -\frac{1}{\varepsilon}\frac{\partial F_y}{\partial x}, \qquad H_z = -j\frac{1}{\omega\mu\varepsilon}\frac{\partial^2 F_y}{\partial y\partial z} \tag{7}$$

The next step is to discuss the fields for two cases, in the groove region and above the corrugations, respectively, and two different modes for each case. At first, we consider the fields within the grooves of TE^y and TM^y modes, and the boundary conditions are as follows:

$$E_x(z=\pm\frac{g}{2})= \text{、} E_x(y=0)=0$$

$$E_y(z=\pm\frac{g}{2})=0\,,E_z(y=0)=0 \tag{8}$$

Also we assume the expression of the vector potential A is as:

$$F_y(x,y,z)=e^{-jk_{x_o}x}[C_y^{\cos}\cos(k_y y)+C_y^{\sin}\sin(k_y y)]\{C_z^{\cos}\cos[k_z(z+\frac{g}{2})]+C_z^{\sin}\sin[k_z(z+\frac{g}{2})]\} \tag{9}$$

Then with (9) substituted into (5) and (7),

$$\begin{bmatrix} E^{groove}_{x_{TE}y} \\ H^{groove}_{x_{TM}y} \end{bmatrix} = -\frac{p\pi}{g}e^{-jk_{x_o}x}\begin{bmatrix} \frac{A^{groove}_{TE}}{\varepsilon_{groove}}S_z S_{y_{TE}} \\ \frac{A^{groove}_{TM}}{\mu_{groove}}C_z C_{y_{TM}} \end{bmatrix} \tag{10a}$$

$$\begin{bmatrix} E^{groove}_{y_{TE}y} \\ H^{groove}_{y_{TM}y} \end{bmatrix} = 0 \tag{10b}$$

$$\begin{bmatrix} E^{groove}_{z_{TE}y} \\ H^{groove}_{z_{TM}y} \end{bmatrix} = jk_{x_o}e^{-jk_{x_o}x}\begin{bmatrix} \frac{A^{groove}_{TE}}{\varepsilon_{groove}}C_z S_{y_{TE}} \\ -\frac{A^{groove}_{TM}}{\mu_{groove}}S_z C_{y_{TM}} \end{bmatrix} \tag{10c}$$

$$\begin{bmatrix} H^{groove}_{x_{TE}y} \\ E^{groove}_{x_{TM}y} \end{bmatrix} = \frac{k_{x_o}e^{-jk_{x_o}x}}{\omega u_{groove}\varepsilon_{groove}}\begin{bmatrix} -A^{groove}_{TE}k^{groove}_{y_{TE}}C_z C_{y_{TE}} \\ A^{groove}_{TM}k^{groove}_{y_{TM}}S_z S_{y_{TM}} \end{bmatrix} \tag{10d}$$

$$\begin{bmatrix} H^{groove}_{y_{TE}y} \\ E^{groove}_{y_{TM}y} \end{bmatrix} = \frac{e^{-jk_{x_o}x}}{j\omega u_{groove}\varepsilon_{groove}}\begin{bmatrix} -A^{groove}_{TE}[k^2_{groove}-(k^{groove}_{y_{TE}})^2]C_z S_{y_{TE}} \\ A^{groove}_{TM}[k^2_{groove}-(k^{groove}_{y_{TE}})^2]S_z C_{y_{TM}} \end{bmatrix} \tag{10e}$$

$$\begin{bmatrix} H^{groove}_{z_{TE}y} \\ E^{groove}_{z_{TM}y} \end{bmatrix} = -\frac{e^{-jk_{x_o}x}\ p\pi/g}{j\omega u_{groove}\varepsilon_{groove}}\begin{bmatrix} A^{groove}_{TE}k^{groove}_{y_{TE}}S_z C_{y_{TE}} \\ A^{groove}_{TM}k^{groove}_{y_{TE}}C_z S_{y_{TM}} \end{bmatrix} \tag{10f}$$

where

$$\begin{bmatrix} C_z \\ S_z \end{bmatrix} = \begin{bmatrix} \cos[\frac{p\pi}{g}(z+\frac{g}{2})] \\ \sin[\frac{p\pi}{g}(z+\frac{g}{2})] \end{bmatrix}, \text{ and } \begin{bmatrix} C_{y_{T\xi}} \\ S_{y_{T\xi}} \end{bmatrix} = \begin{bmatrix} \cos(k^{groove}_{y_{T\xi}}y) \\ \sin(k^{groove}_{y_{T\xi}}y) \end{bmatrix}$$

in which ξ may be the E or H, and p is the 0,1,2….

Next we discuss the fields in the region above corrugations (y > d), and assume its vector potential A is as follows:

$$A_y^{above}(x, y > d, z) = A_{TM}^{above}\, \mathrm{e}^{-jk_{x_o}x}\, e^{-jk_{y_{TM}}^{above}(y-d)}\, e^{-jk_{z_{TM}}^{above}z} \tag{11}$$

Then using (5) and (7) to substitute for (11)

$$\begin{bmatrix} E_{x_{TE^y}}^{above} \\ E_{z_{TE^y}}^{above} \end{bmatrix} = \frac{A_{TE}^{above}\, j\, \mathrm{e}^{-jk_{x_o}x}\, e^{-jk_{y_{TE}}^{above}(y-d)}\, e^{-jk_{z_{TE}}^{above}z}}{\varepsilon_{above}} \begin{bmatrix} -k_{z_{TE}}^{above} \\ k_{x_o} \end{bmatrix} \tag{12a}$$

$$\begin{bmatrix} E_{y_{TE^y}}^{above} \\ H_{y_{TM^y}}^{above} \end{bmatrix} = 0 \tag{12b}$$

$$\begin{bmatrix} H_{x_{TE^y}}^{above} \\ H_{y_{TE^y}}^{above} \\ H_{z_{TE^y}}^{above} \end{bmatrix} = \frac{A_{TE}^{above}\, \mathrm{e}^{-jk_{x_o}x}\, e^{-jk_{y_{TE}}^{above}(y-d)}\, e^{-jk_{z_{TE}}^{above}z}}{j\omega\mu_{above}\varepsilon_{above}} \begin{bmatrix} -k_{x_o} k_{y_{TE}}^{above} \\ k_{above}^2 - (k_{y_{TE}}^{above})^2 \\ -k_{y_{TE}}^{above} k_{z_{TE}}^{above} \end{bmatrix} \tag{12c}$$

$$\begin{bmatrix} E_{x_{TM^y}}^{above} \\ E_{y_{TM^y}}^{above} \\ E_{z_{TM^y}}^{above} \end{bmatrix} = \frac{A_{TM}^{above}\, \mathrm{e}^{-jk_{x_o}x}\, e^{-jk_{y_{TM}}^{above}(y-d)}\, e^{-jk_{z_{TM}}^{above}z}}{j\omega\mu_{above}\varepsilon_{above}} \begin{bmatrix} -k_{x_o} k_{y_{TM}}^{above} \\ k_{above}^2 - (k_{y_{TM}}^{above})^2 \\ -k_{y_{TM}}^{above} k_{z_{TM}}^{above} \end{bmatrix} \tag{12d}$$

$$\begin{bmatrix} H_{x_{TM^y}}^{above} \\ H_{z_{TM^y}}^{above} \end{bmatrix} = \frac{A_{TE}^{above}\, j\, \mathrm{e}^{-jk_{x_o}x}\, e^{-jk_{y_{TM}}^{above}(y-d)}\, e^{-jk_{z_{TM}}^{above}z}}{\mu_{above}} \begin{bmatrix} k_{z_{TM}}^{above} \\ -k_{x_o} \end{bmatrix} \tag{12e}$$

The unit vectors parallel and orthogonal to the corrugations are defined as $\hat{a}_p$ and $\hat{a}_o$, respectively. According to [12], the asymptotic corrugation boundary conditions are stated as follows:

$$\vec{E}_{groove} \cdot \hat{a}_p = 0 \tag{13a}$$

$$\vec{E}^{above} \cdot \hat{a}_p = 0 \tag{13b}$$

$$\vec{E}_{groove} \cdot \hat{a}_o = \vec{E}^{above} \cdot a_o \tag{13c}$$

$$\vec{H}_{groove} \cdot \hat{a}_p = \vec{H}^{above} \cdot a_p \tag{13d}$$

Assuming p_{TE}=0 and p_{TM}=0, i.e. we only consider the dominant mode of TE and absence

of all the TM modes. When p_{TE}=0, $E_{x_{TE^y}}^{groove}=0$ in (10a), meanwhile $E_{x_{TM^y}}^{groove}=0$ when we ignore the TM modes, so the boundary conditions of (13a) is automatically satisfied. As for (13b), we require

$$E_{x_{TE^y}}^{above}(y=d)+E_{x_{TM^y}}^{above}(y=d)=0 \tag{14}$$

For phase continuity, we can get $k_x^{univ}=k_{x0}$ and $k_z^{univ}=k_{z_{TM}}^{above}=k_{z_{TE}}^{above}$. So we can obtain

$$-A_{TE}^{above}\frac{jk_z^{univ}}{\varepsilon_{abv}}\cancel{e^{-jk_x^{univ}x}e^{-jk_z^{univ}z}}-A_{TM}^{above}\frac{k_x^{univ}k_{y_{TM}}^{above}}{j\omega\mu_{abv}\varepsilon_{abv}}\cancel{e^{-jk_x^{univ}x}e^{-jk_z^{univ}z}}=0 \tag{15a}$$

Then

$$A_{TM}^{above}=\frac{\omega\mu_{above}k_z^{univ}}{k_x^{univ}k_{y_{TM}}^{above}}A_{TE}^{above} \tag{15b}$$

As for (13c), we require

$$E_{z_{TE^y}}^{groove}(y=d)\Big|_{p_{TE}=0}+E_{z_{TM^y}}^{groove}(y=d)\Big|_{p_{TM}=0}=E_{z_{TE^y}}^{above}(y=d)+E_{z_{TM^y}}^{above}(y=d) \tag{16}$$

in which the second term on left hand side is vanished since we assumed that no TM modes exist within the groove. Using (10c), (12a), and (12d) to substitute in (16)

$$\begin{aligned}&\sum_i A_{TE}^{groove}\frac{jk_{x0}}{\varepsilon_{groove}}e^{-jk_x^{univ}x}\sin\left(k_{y_{TE}}^{groove}d\right)e^{-jk_z^{univ}id_z}\\ &\underset{d_z\to 0}{\simeq}A_{TE}^{above}\frac{jk_{x0}}{\varepsilon_{abv}}e^{-jk_x^{univ}x}e^{-jk_z^{univ}z}-A_{TM}^{above}\frac{k_{y_{TM}}^{above}k_z^{univ}}{j\omega\mu_{abv}\varepsilon_{abv}}e^{-jk_x^{univ}x}e^{-jk_z^{univ}z}\end{aligned} \tag{17}$$

where i is the groove index, noting how the left-hand side quantity varies with z in a stepwise manner, with each term of its summation being a piecewise constant within the i^{th} groove, i.e. $id_z - g/2 < z < id_z + g/2$. Now we only focus on the ith groove, so the summation over the groove index on the left-hand side is removed, resulting in

$$A_{TE}^{groove}\frac{jk_{x0}}{\varepsilon_{groove}}\sin\left(k_{y_{TE}}^{groove}d\right)e^{-jk_z^{univ}id_z}\underset{d_z\to 0}{\simeq}\left(A_{TE}^{above}\frac{jk_{x0}}{\varepsilon_{abv}}-A_{TM}^{above}\frac{k_{y_{TM}}^{above}k_z^{univ}}{j\omega\mu_{abv}\varepsilon_{abv}}\right)e^{-jk_z^{univ}z}\Big|_{id_z-\frac{g}{2}<z<id_z+\frac{g}{2}} \tag{18}$$

And as the period d_z tends to zero, the $e^{-jk_z^{univ}z}$ factor on the right-hand side of (18) becomes approximately $e^{-jk_z^{univ}id_z}$. This expresses that the continuous variation with z can be approximated as a piecewise discrete constant over the i^{th} groove of nearly zero width. Hence the resultant $e^{-jk_z^{univ}id_z}$ gets canceled out on both sides, leading to

$$A_{TE}^{groove}\frac{jk_{x0}}{\varepsilon_{groove}}\sin\left(k_{y_{TE}}^{groove}d\right)=A_{TE}^{above}\frac{jk_{x0}}{\varepsilon_{abv}}-A_{TM}^{above}\frac{k_{y_{TM}}^{above}k_z^{univ}}{j\omega\mu_{abv}\varepsilon_{abv}} \tag{19a}$$

Using (15b) to substitute for A_{TM}^{above} in (19a), yielding

$$A_{TE}^{groove}\frac{k_{x_o}^2}{\varepsilon_{groove}}\sin\left(k_{y_{TE}}^{groove}d\right)=A_{TE}^{above}\frac{k_{x_o}^2+(k_z^{univ})^2}{\varepsilon_{above}} \tag{19b}$$

As for (13d), we require

$$H_{x_{TE}^y}^{groove}(y=d)\Big|_{p_{TE}=0}+H_{x_{TM}^y}^{groove}(y=d)\Big|_{p_{TM}=0}=H_{x_{TE}^y}^{above}(y=d)+H_{x_{TM}^y}^{above}(y=d) \tag{20}$$

in which again the second term on the left hand side is vanished.

To replace (20) in (10a), (10d, and (12e)

$$\begin{aligned}&-\sum_i A_{TE}^{groove}\frac{k_{x0}k_{y_{TE}}^{groove}}{\omega\mu_{groove}\varepsilon_{groove}}e^{-jk_x^{univ}x}\cos\left(k_{y_{TE}}^{groove}d\right)e^{-jk_z^{univ}id_z}\\ &\underset{d_z\to 0}{\simeq}-A_{TE}^{above}\frac{k_{x0}k_{y_{TE}}^{above}}{j\omega\mu_{abv}\varepsilon_{abv}}e^{-jk_x^{univ}x}e^{-jk_z^{univ}z}+A_{TM}^{above}\frac{jk_z^{univ}}{\mu_{abv}}e^{-jk_x^{univ}x}e^{-jk_z^{univ}z}\end{aligned} \tag{21}$$

And as the same process from (17) to (19), we can modify (21), leading to

$$-A_{TE}^{groove}\frac{k_{x0}k_{y_{TE}}^{groove}}{\omega\mu_{groove}\varepsilon_{groove}}\cos\left(k_{y_{TE}}^{groove}d\right)=-A_{TE}^{above}\frac{k_{x0}k_{y_{TE}}^{above}}{j\omega\mu_{abv}\varepsilon_{abv}}+A_{TM}^{above}\frac{jk_z^{univ}}{\mu_{abv}} \tag{22a}$$

Using (15b) to substitute for A_{TM}^{above} in (22a), yielding

$$A_{TE}^{groove}\frac{k_{x0}k_{y_{TE}}^{groove}}{\omega\mu_{groove}\varepsilon_{groove}}\cos\left(k_{y_{TE}}^{groove}d\right)=-\frac{jA_{TE}^{above}}{\mu_{above}}\frac{k_{x_o}^2k_{y_{TE}}^{above}k_{y_{TM}}^{above}+\omega^2\mu_{above}\varepsilon_{above}(k_z^{univ})^2}{\omega\varepsilon_{above}k_{x_o}k_{y_{TM}}^{above}} \tag{22b}$$

As observed, we can see that since the left hand side is pure real ($k_{y_{TE}}^{groove}$ is real), the right hand side must be real. In order for this, the $k_{y_{TE}}^{above}$ and $k_{y_{TM}}^{above}$ must be pure imaginary such that their product in numerator becomes real, whereas the remaining $k_{y_{TM}}^{above}$ in denominator causes the whole right hand side equation to be imaginary. This conforms with what we expect of $k_{y_{TE}}^{above}$ and $k_{y_{TM}}^{above}$, being wavenumbers along vertical direction perpendicularly away from corrugation xz-surface, which should be indeed be imaginary in order for surface wave along xz plane surface of corrugation, i.e. decaying fields as one observe perpendicularly away from corrugation surface. Hence

$$k_{y_{TE}}^{above} = -j\alpha_{y_{TE}}^{above} \text{ and } k_{y_{TM}}^{above} = -j\alpha_{y_{TM}}^{above} \tag{23}$$

Thus, with two replacement made, (22b) becomes

$$A_{TE}^{groove} \frac{k_{x0} k_{y_{TE}}^{groove}}{\omega \mu_{groove} \varepsilon_{groove}} \cos\left(k_{y_{TE}}^{groove} d\right) = A_{TE}^{above} \frac{k_{above}^2 (k_z^{univ})^2 - k_{x_o}^2 \alpha_{y_{TE}}^{above} \alpha_{y_{TM}}^{above}}{\mu_{above} \varepsilon_{above} k_{x_o} \alpha_{y_{TM}}^{above}} \tag{24}$$

Dividing (19b) by (24)

$$\frac{\mu_{groove} k_{x_o}}{k_{y_{TE}}^{groove}} \tan(k_{y_{TE}}^{groove} d) = \frac{\mu_{above} k_{x_o} \alpha_{y_{TM}}^{above} \left[k_{x_o}^2 + \left(k_z^{univ}\right)^2\right]}{k_{above}^2 \left(k_z^{univ}\right)^2 - k_{x_o}^2 \alpha_{y_{TE}}^{above} \alpha_{y_{TM}}^{above}} \tag{25}$$

The general formula for $k_{y_{TE}}^{groove}$ is given by

$$k_{y_{TE}}^{groove} = \sqrt{\omega^2 \mu_{groove} \varepsilon_{groove} - \left(k_x^{univ}\right)^2 - \left(k_z^{groove}\right)^2} \tag{26a}$$

Again we only consider the dominant mode under ACBC, which means $p_{TE}=p_{TM}=0$, so k_z^{groove} is zero, i.e.

$$k_z^{groove} = p_{TE}\pi / g = p_{TM}\pi / g = 0, \text{ under ACBC} \tag{26b}$$

So (26a) becomes

$$k_{y_{TE}}^{groove} = \sqrt{\omega^2 \mu_{groove} \varepsilon_{groove} - \left(k_x^{univ}\right)^2}, \text{ under ACBC} \tag{26c}$$

We may equate both TE and TM attenuation constants along the vertical y direction for the upper half-space region above corrugation as the explanation just after (14), yielding

$$\alpha_{y_{TE}}^{above} = \alpha_{y_{TM}}^{above} \underset{say}{=} \alpha_y^{above} \tag{26d}$$

With

$$\left(\alpha_y^{above}\right)^2 = \left(k_x^{univ}\right)^2 + \left(k_z^{univ}\right)^2 - \omega^2 \mu_{abv} \varepsilon_{abv} \tag{26e}$$

At last, based on (26a) to (26e), we can modify (25) as

$$\frac{\mu_{above}\left[k_{x_o}^2 + \left(k_z^{univ}\right)^2\right]\sqrt{k_{x_o}^2 + \left(k_z^{univ}\right)^2 - k_{above}^2}}{k_{above}^2 \left(k_z^{univ}\right)^2 - \left[k_{x_o}^2 + \left(k_z^{univ}\right)^2 - k_{above}^2\right]} - \frac{\mu_{groove}}{\sqrt{k_{groove}^2 - k_{x_o}^2}} \tan\left(\sqrt{k_{groove}^2 - k_{x_o}^2}\, d\right) = 0 \tag{27}$$

where

$$k_{groove} = 2\pi f \sqrt{\mu_{groove} \varepsilon_{groove}}, k_{above} = 2\pi f \sqrt{\mu_{abv} \varepsilon_{abv}} \tag{28}$$

Eq.(27) is the characteristic equation of the corrugation.

2-2 Refinement factor of the characteristic equation

The surface impedance looking down at y=d towards the PEC floor of the corrugations is defined as follows:

$$Z_{s\downarrow}^{groove\ TE} = -\frac{E_{z_{TE^y}}^{groove}(y=d)}{H_{x_{TE^y}}^{groove}(y=d)} \tag{29a}$$

substituting (10a) and (10f) into (29a), yielding

$$Z_{s\downarrow}^{groove\ TE} = j\frac{\omega\mu_{groove}}{k_{y_{TE}}^{groove}}\tan\left(k_{y_{TE}}^{groove}d\right) \tag{29b}$$

where $\omega\mu_{groove}/k_{y_{TE}}^{groove}$ is the familiar TEy modal impedance Z_c^{TE}, therefore obtaining the familiar input impedance of a shorted transmission line of length d.

Similarly, the input impedance looking up at y=d interface into the upper-half space is:

$$Z_{s\uparrow}^{above\ TE} = -\frac{E_{x_{TE^y}}^{above}(y=d)}{H_{z_{TE^y}}^{above}(y=d)} = \frac{E_{z_{TE^y}}^{above}(y=d)}{H_{x_{TE^y}}^{above}(y=d)} = \frac{j\omega\mu_{abv}}{\sqrt{\left(k_x^{univ}\right)^2+\left(k_z^{univ}\right)^2-k_{above}^2}} = \frac{j\omega\mu_{abv}}{\gamma_y^{above}} \tag{30}$$

being the familiar TE modal impedance, where as

$$Z_{s\uparrow}^{above\ TM} = -\frac{E_{x_{TM^y}}^{above}(y=d)}{H_{z_{TM^y}}^{above}(y=d)} = \frac{E_{z_{TM^y}}^{above}(y=d)}{H_{x_{TM^y}}^{above}(y=d)} = \frac{\sqrt{\left(k_x^{univ}\right)^2+\left(k_z^{univ}\right)^2-k_{above}^2}}{j\omega\varepsilon_{abv}} = \frac{\gamma_y^{above}}{j\omega\varepsilon_{abv}} \tag{31}$$

being the familiar TM modal impedance.

The whole E_x and E_z in the numerators of the expressions for these impedances seems exist, but actually it is only under the ACBC conditions. As mentioned, ACBC is an approximate method to analyze corrugation, and its hypothesis is that we assume the ridge is tending to zero. For the real case, there exist widths for the ridges, so (27) may produce some errors in its results compared to the simulation or measurement The E_x and E_z vanish over the top PEC surfaces of the metallic ridge, hence, it is fairly presumed that the E^{above} fields on the corrugation surface may be corrected by an incremental (> 1) factor d_z/g, where d_z is the corrugation period and g is the groove-width. By doing this, in reality, the E^{above} fields on the corrugation surface with the reduction factor (< 1) (as required by the fractional existence of the tangential E-field components over only apertures of the grooves, and vanishing over the ridge-top) will neutralize that aforementioned incremental factor, thereby maintaining the abovementioned impedances, since there is no for these impedances to be changed.

The equation containing E^{above} should all be modified, which are (14) and (16), and it can be seen that this multiplicative correction factor would get canceled throughout (14), meaning that only (16) should be modified, which is

$$E_{z_{TE^y}}^{groove}(y=d)=\frac{d_z}{g}\left[E_{z_{TE^y}}^{above}(y=d)+E_{z_{TM^y}}^{above}(y=d)\right] \tag{32a}$$

again using (10c), (12a), and (12d) to substitute in (32a), obtaining

$$A_{TE}^{groove}\frac{jk_{x0}}{\varepsilon_{groove}}\sin\left(k_{y_{TE}}^{groove}d\right)-A_{TE}^{above}\frac{d_z}{g}\frac{jk_{x0}}{\varepsilon_{abv}}+A_{TM}^{above}\frac{d_z}{g}\frac{k_{y_{TM}}^{above}k_z^{univ}}{j\omega\mu_{abv}\varepsilon_{abv}}=0 \tag{32b}$$

so the last characteristic equation is also changed to

$$\frac{d_z}{g}\frac{\mu_{above}\left[k_{x_o}^2+\left(k_z^{univ}\right)^2\right]\sqrt{k_{x_o}^2+\left(k_z^{univ}\right)^2-k_{above}^2}}{k_{above}^2\left(k_z^{univ}\right)^2-\left[k_{x_o}^2+\left(k_z^{univ}\right)^2-k_{above}^2\right]}-\frac{\mu_{groove}}{\sqrt{k_{groove}^2-k_{x_o}^2}}\tan\left(\sqrt{k_{groove}^2-k_{x_o}^2}\,d\right)=0 \tag{33}$$

Depending on which two of the following three quantities: (i) frequency $f = \omega/(2\pi)$, (ii) k_x^{univ}, and (iii) k_z^{univ} we choose, the third quantity remains as the only unknown in this (33), which may then be solved for as roots of this characteristic equation. Doing so yields the required information for plotting various path-regions of the dispersion diagram (O→Z, Z→M, M→X, or X→O). If we know the frequency and set k_x^{univ} as zero, we can get the root of k_z^{univ}, which is the O→Z of the dispersion diagram, where Z refers to the Brillouin limit, π / d_z. Similarly, setting the k_z^{univ} as Brillouin limits, and solve the root for, we can get Z→M part. The dispersion diagrams generated by the present ACBC-based method are compared with commercial full-wave simulator software: CST Microwave Studio®. Two arbitrary examples shall be studied as follow.

2-3-1 An arbitrary example

The parameters are as follow: period d_z = 2mm, groove-width g = 0.85*d_z, depth d = 8mm, $\varepsilon_{rel,groove}$ = 2 and $\mu_{rel,groove}$ = 1. As seen, the roots of the characteristic equation produce a dispersion trace which takes on the form of cyclic 'peaking' of the k_z^{univ} at various resonant frequencies in Fig. 4(a). Moreover, the trace just 'grazes' the light-line, i.e. it is tangent to it, occurring at frequencies slightly above those whereby the trace has dropped back to its local minima and begun to rise again. In fact, the backward trace of the dispersion diagram in Fig. 4(a) is not exist, the reason why it appears is because the magnitude of the 'backward' part is small, and even though it is small, the algorithm we used in Matlab still can detect these roots. The comparison to the CST simulation results will be shown in the next section, and we will see that no backward trace is shown in the simulation results.

Interesting aspect is now pointed out. The frequencies at which the peaks occur coincide perfectly with the so-called "soft" frequencies [3] of the corrugations, defined as

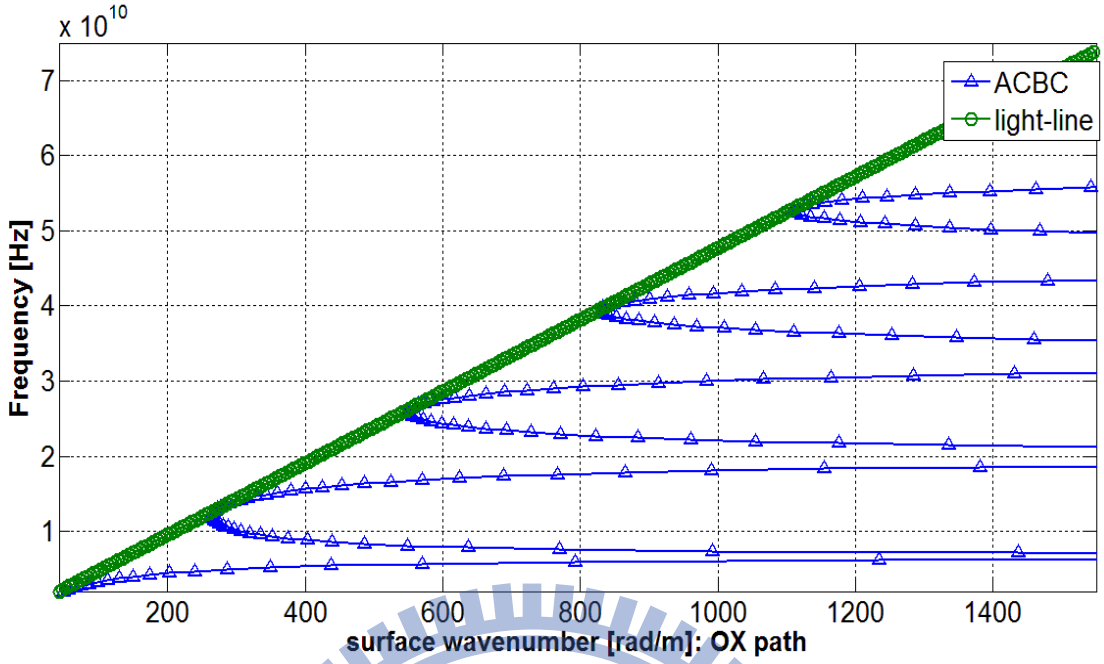

Figure 4 (a): O→Z path of the dispersion diagram

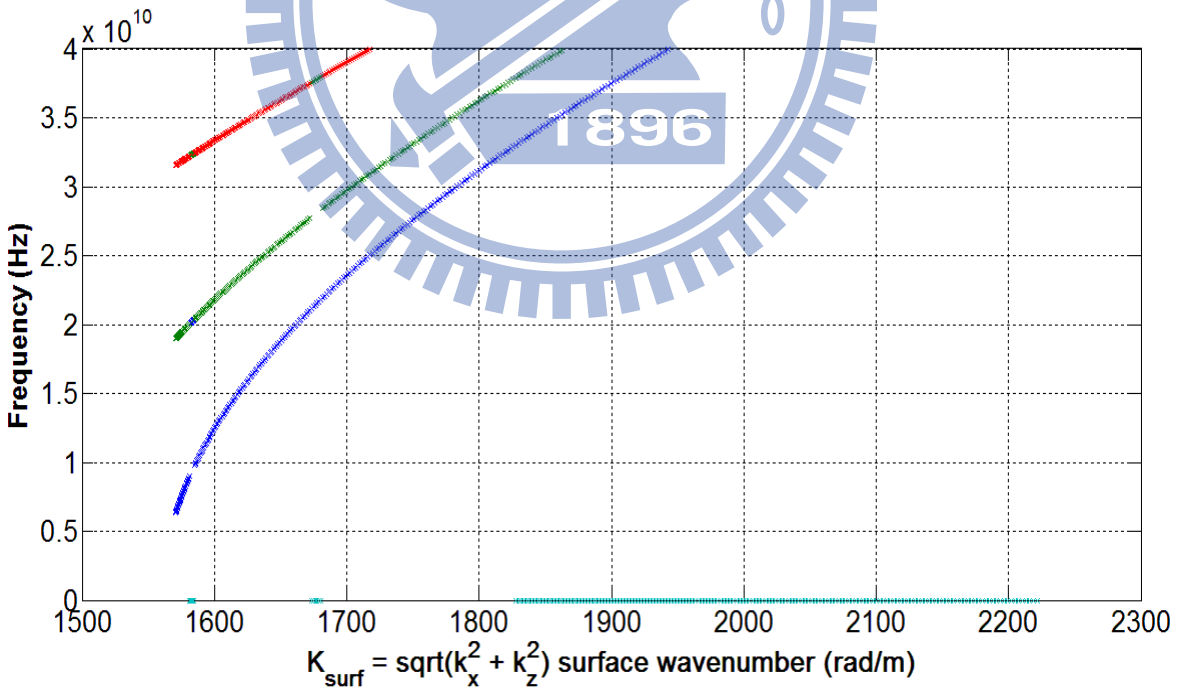

Figure 4 (b): Z→M path of the dispersion diagram

$$f_n^{soft} = c(2n+1) \Big/ \left(4d_{soft}\sqrt{\varepsilon_{rel,groove}}\right) \tag{34}$$

where n is an integer representing the order of the soft boundary condition, c is the speed of light in vacuum, d_{soft} is the depth of the corrugations at which the soft boundary condition holds, and $\varepsilon_{rel,groove}$ is the relative permittivity of the dielectric filling the grooves.

2-3-2 ACBC method compared to CST

The parameters are as follow: period of the unit cell d_z = 3mm, groove-width g = 0.55*d_z, depth d = 4mm, $\varepsilon_{rel,groove}$ = 3 and $\mu_{rel,groove}$ = 1. The dispersion diagram obtained in this section is from Eq. (38), which are corrected characteristic equation, but not Eq. (27), and we will see the good match between the corrected ACBC methods and CST. The comparison between the uncorrected and corrected ACBC methods will be discussed in the next section. As additional results and still on this second example, the dispersion graphs for three other paths of the typical "O→X→M→Y→O" dispersion diagram typical of two-dimensional periodic EBG structures are given in Figs. 5(b), 5(c), and 5(d), providing the "X→M", "M→Y", and "Y→O" (Z→M, M→X, and X→O for the present example) portions, respectively. However, for the present case of corrugations, there is actually no periodicity in the direction (x here) along them. Nonetheless, we shall still set the Brillouin limit along this direction as π divided by the same period (along z) of the corrugations, thus assuming a square unit cell (although strictly, the unit cell is an infinitely long strip in the zx plane of the corrugations, infinitely long along x, the orientation of the corrugations). For the "O→X" (O→Z for the present example) part shown in Fig. 5(a), as observed, only the rising parts of the 'peaking' trace after the 'grazing' are relevant, which is because just as mentioned, the algorithm we use may detect some small deviated data which are negligible. But the comparisons between the present ACBC method and CST for all three graphs of Fig. 5(b) through 5(d) demonstrate fine agreement, thereby further substantiating the present technique.

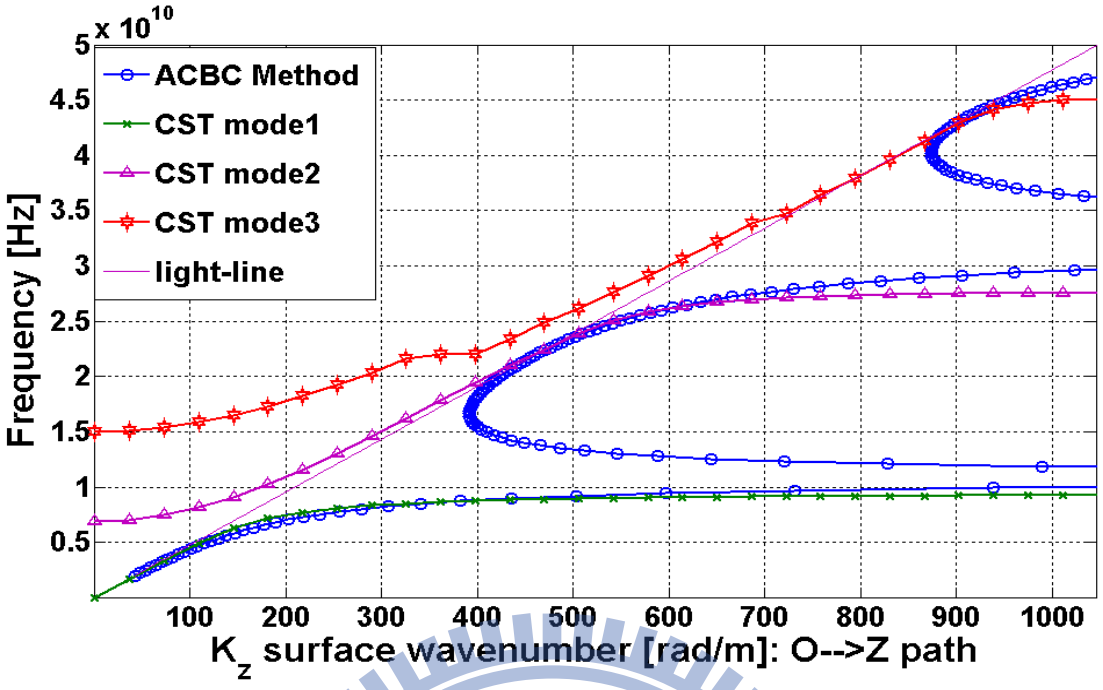

Figure 5 (a): Comparison between the CST simulation results and corrected ACBC method for O→Z path.

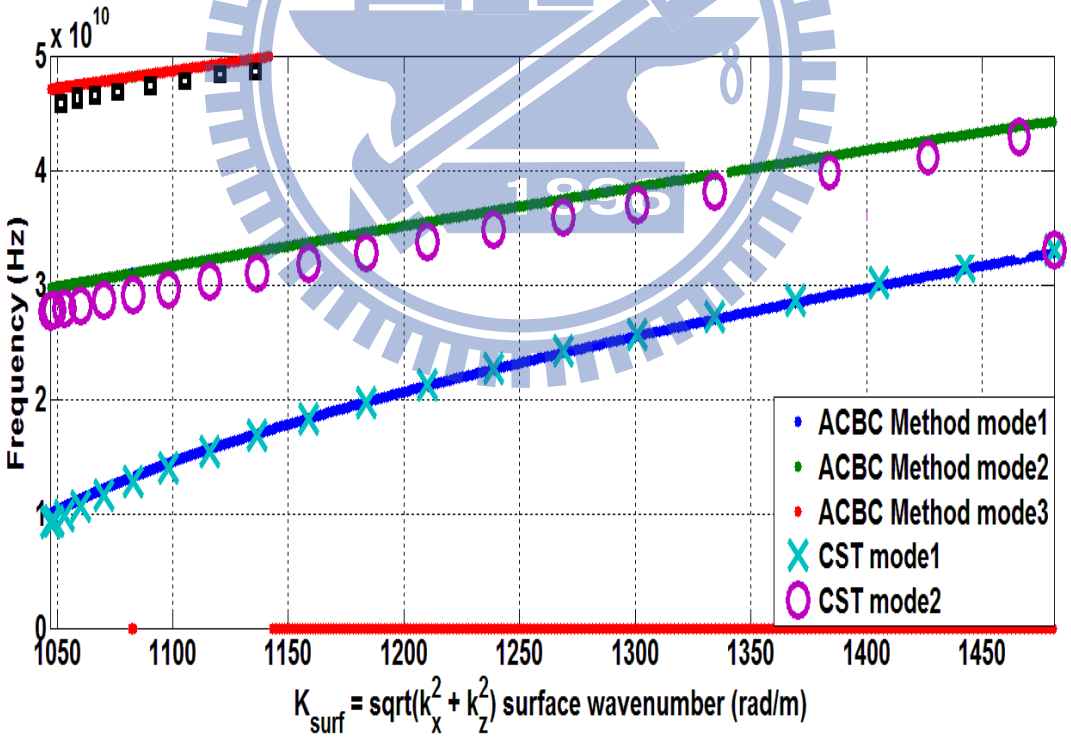

Figure 5 (b): Comparison between the CST simulation results and corrected ACBC method for Z→M path.

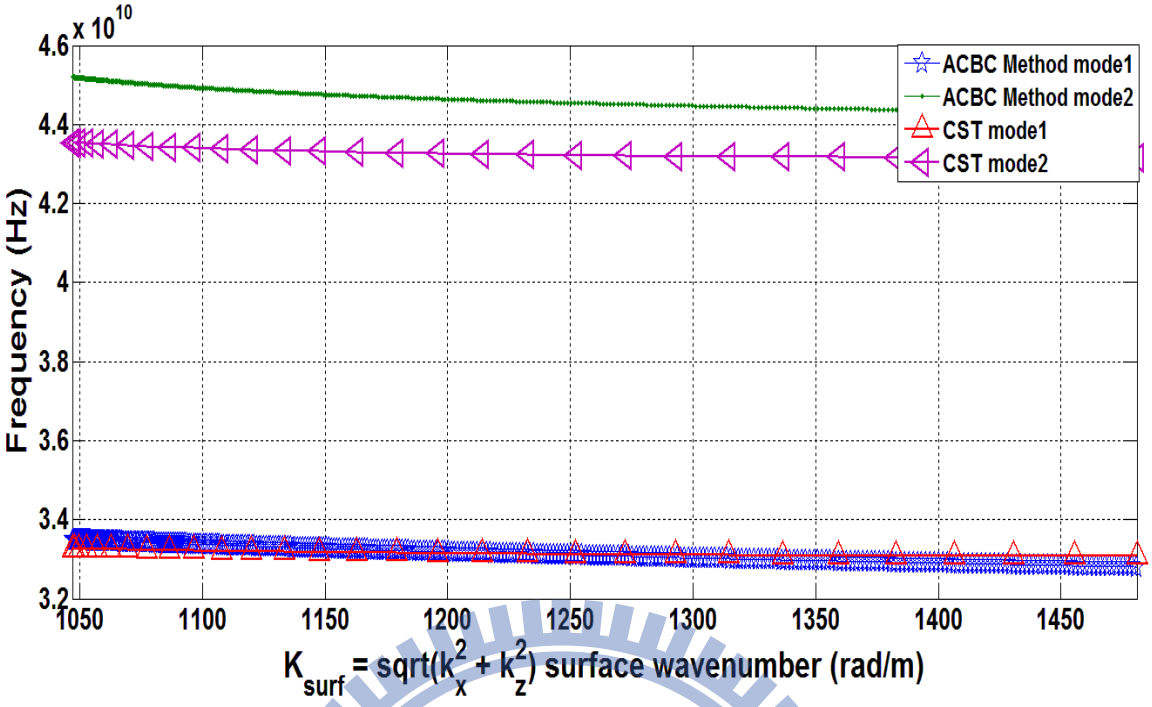

Figure 5 (c): Comparison between the CST simulation results and corrected ACBC method for M→X path.

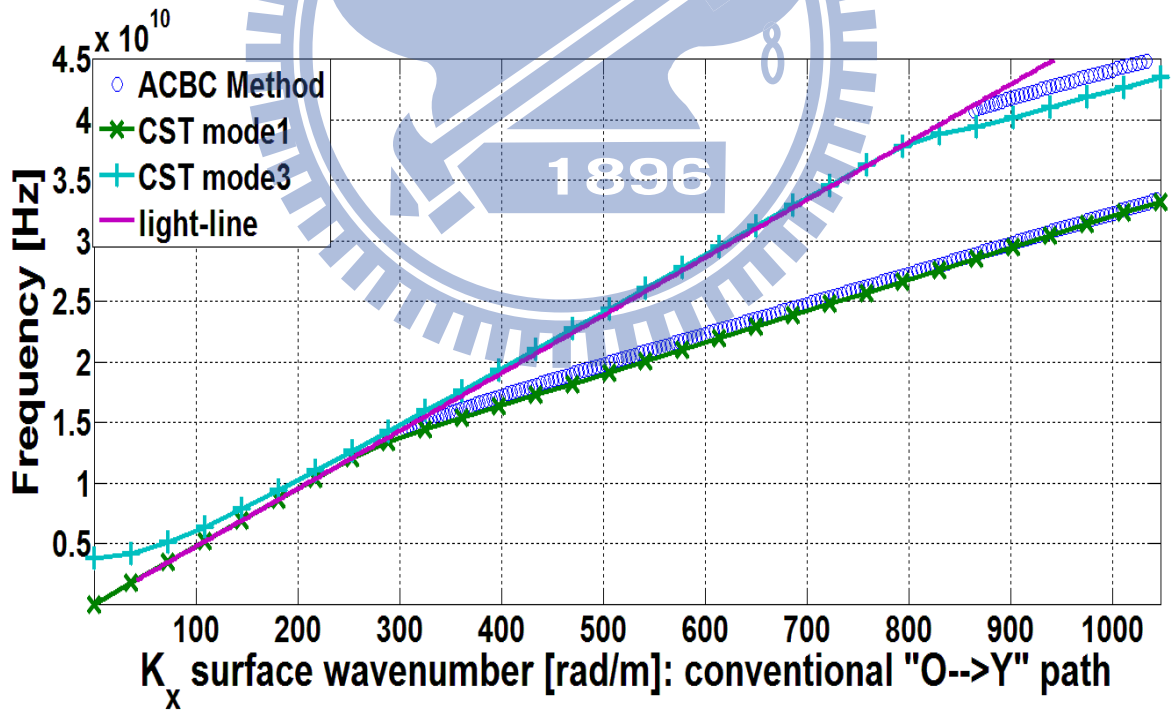

Figure 5 (d): Comparison between the CST simulation results and corrected ACBC method for O→X path (conventional O→Y path.).

2-4 Influence of refinement factor

In this section, the accuracy of the refinement factor for the characteristics equation will be shown, and we study the O→Z part first. The parameters we choose are as follows: d_z = 1mm, d = 5mm, $\varepsilon_{rel,groove}$ = 3, $\mu_{rel,groove}$ = 1, and comparing two different example which are g/d_z =0.2 and g/d_z =0.7. Just as mentioned, ACBC is an "approximate" method to analyze the corrugation, and the approximation is that ridge tends to be zero. In other words, if the width of the ridge is larger in a period, the result showed by uncorrected ACBC methods will be more inaccurate, so that is why we need the refinement factor. Fig. 6(a) and Fig. 6(b) show the comparison of the dispersion diagram for the O→Z part resulting from Eq. (27) (uncorrected ACBC methods) and Eq. (33) (corrected ACBC methods), and both are discussed in two cases which are g/d_z =0.2mm and g/d_z =0.7mm, respectively. Since the accuracy of the corrected ACBC methods has been proven in the last section, it will be used as a standard here. It can be seen that no matter what value of g/d_z is, it does not affect the dispersion diagram resulting from ACBC method without correction method, and for which is not so practical. As the groove width gets smaller, which means the condition gets farther than the uncorrected ACBC, the improvement effects from the correction factor gets better. The similar situations also happened to the Z→M part, which are shown in Fig 7(a) and Fig 7(b). In fact, from our simulation results for the entire parametric space, we found that the accuracy

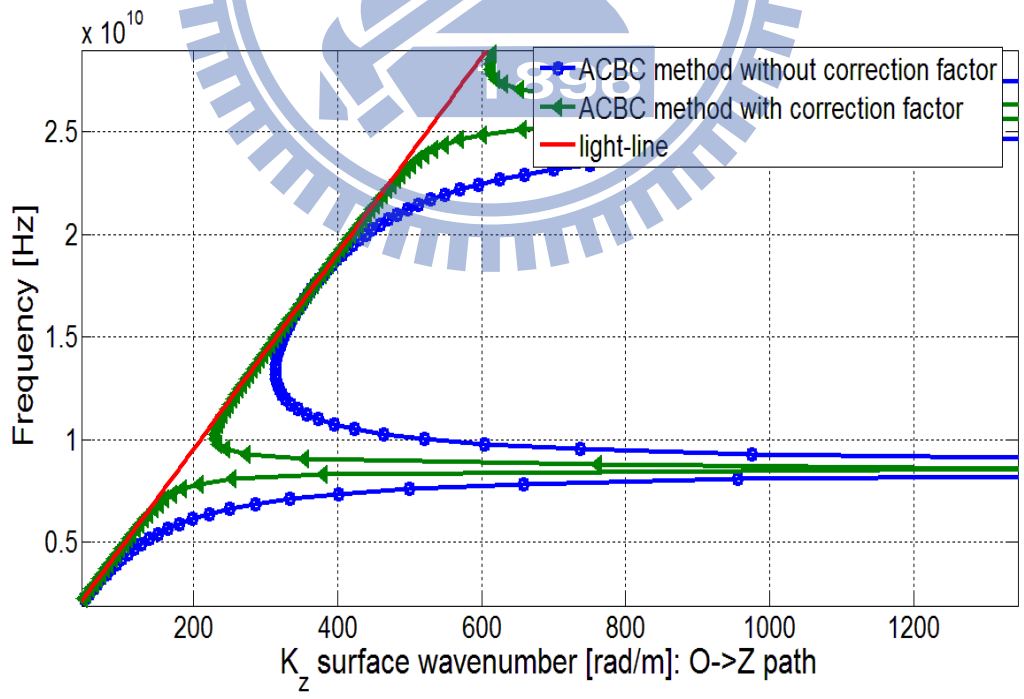

Figure 6(a): Comparison between the uncorrected and corrected ACBC method for O→Z path as the g/d_z =0.2.

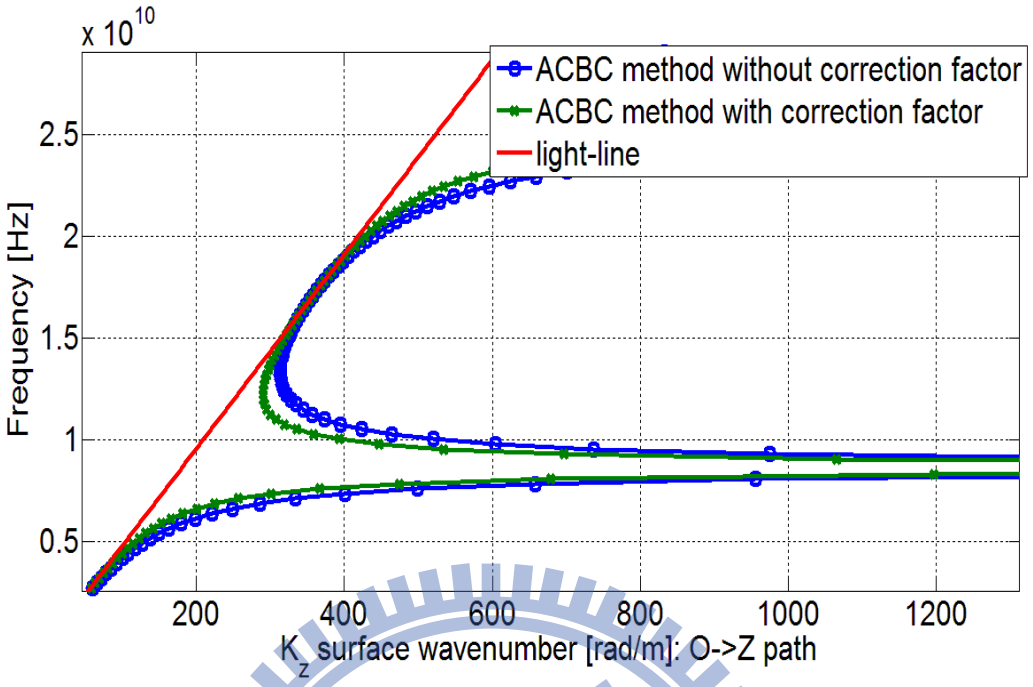

Figure 6(b): Comparison between the uncorrected and corrected ACBC method for O→Z path as the g/d_z =0.7.

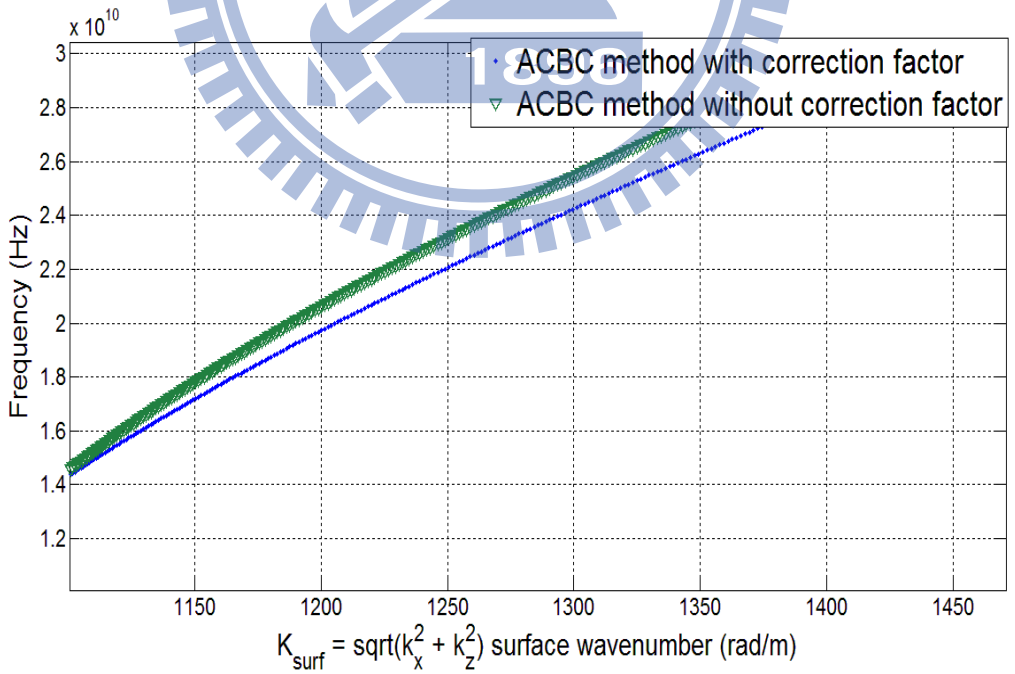

Figure 7(a): Comparison between the uncorrected and corrected ACBC methods for Z→M path as the g/d_z =0.2.

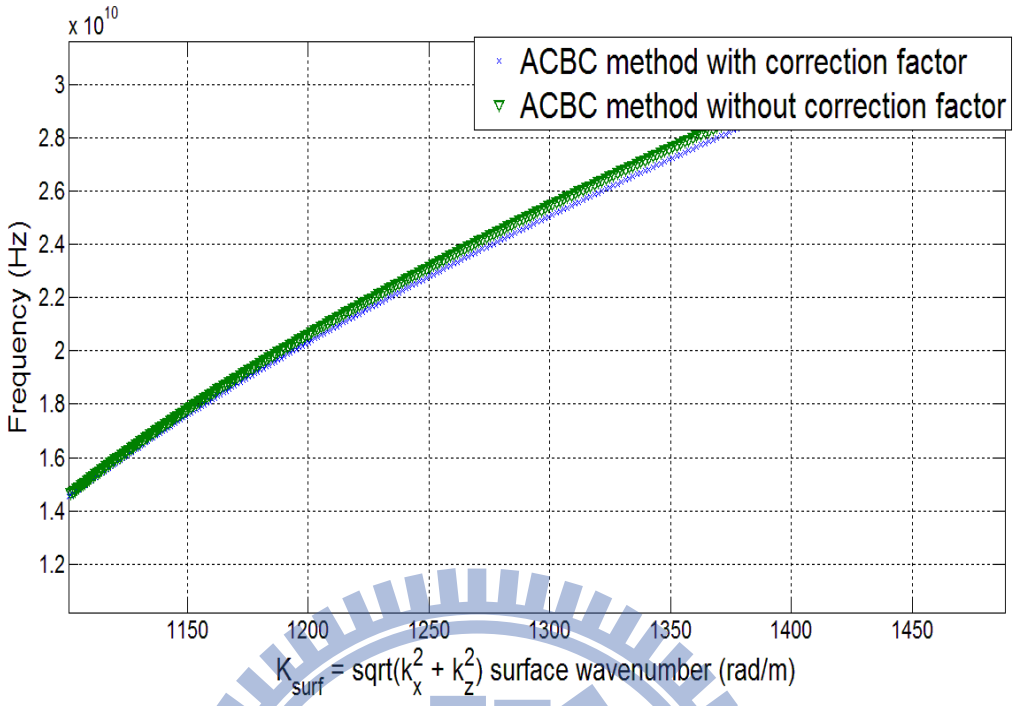

Figure 7(b): Comparison between the uncorrected and corrected ACBC methods for Z→M path as the g/d_z =0.7.

of the unrefined ACBC method is properly satisfactory when g/d_z is greater than 0.7, but degrades rapidly as the ratio falls below this threshold value, for which the refined dispersion relation of Eq. (33) would then be required.

2-5 ACBC method compared to TRT

Actually, the dispersion diagram of the corrugation has been investigated decades ago, which is transverse resonant technique (TRT). The characteristic equation is obtained by matching impedance in [15], whereas with the assumption that only the TM modal exist for y>d. We will briefly introduce how its characteristic equation comes.

The impedance looking upward is that of a TM wave propagating in the y-direction, yielding

$$Z_{upward} = \frac{k_y}{\omega \varepsilon_o} \tag{35}$$

the impedance looking down into the corrugation would be

$$Z_{downward} = \frac{jW}{W+t}\sqrt{\frac{\mu_r}{\varepsilon_r}}\tan\left(k_{groove}d\right) \tag{36}$$

where W is the period and t is the ridge width, We can see that (36) is quite similar to (29b),

the former one is for TM modal while the latter one is for TE modal, and also (36) has already considered the incremental factor $\frac{W}{W+t}$.

So by TRT theory, matching impedance at y=d requires that

$$Z_{upward} = -Z_{downward} \tag{37}$$

resulting in

$$k_z = \sqrt{4(\pi f)^2 \mu_0 \varepsilon_0 + 4\mu_0 \varepsilon_0 \left(\frac{W\pi f}{W+t}\right)^2 \frac{\mu_{rg}}{\varepsilon_{rg}} \tan^2\left(2\pi f d\sqrt{\mu_g \varepsilon_g}\right)} \tag{38}$$

for O→Z part. And

$$\frac{W\sqrt{4(\pi f)^2 \mu_0 \varepsilon_0 - k_x^2}}{W+t} \frac{\mu_{rg}}{\varepsilon_{rg}} \tan\left(d\sqrt{\mu_{rg}\varepsilon_{rg}\left[4(\pi f)^2 \mu_0 \varepsilon_0 - k_x^2\right]}\right) = \sqrt{k_z^2 + k_x^2 - 4(\pi f)^2 \mu_0 \varepsilon_0} \tag{39}$$

for Z→M part.

Figs. 8 show the comparison between the ACBC method and TRT method which is from the book written by Carlton H Walter. The dimension is the same as Fig. 5(a). We can see from Fig. 8(a), for O→Z part, TRT method matches well to the corrected ACBC methods, and also the information is obtained that corrected ACBC method really improves the accuracy for the uncorrected ACBC method (since we have already proved in Fig. 5(a) that corrected ACBC method matches well to the CST software, we use the former one as the standard). Just like the ACBC method, the cyclical 'peaking' of the k_z at various resonant frequencies is also exhibited by the TRT, and its traces also just 'graze' the light-line, i.e. are tangent to it.

However, Fig. 8(b) for oblique surface-wave propagation reveals that the TRT leads to severe errors in the dispersion diagrams. Only at the Bragg condition (Brillouin limit), i.e. left edge of Fig. 8(b) that links to the right edge of Fig. 8(a), will the accuracy of the TRT be satisfactory, but degrades rapidly as the surface wave vector departs from the principal direction. For such acute inaccuracies, even the uncorrected ACBC method of (27) provides better characterization of oblique surface wave propagation.

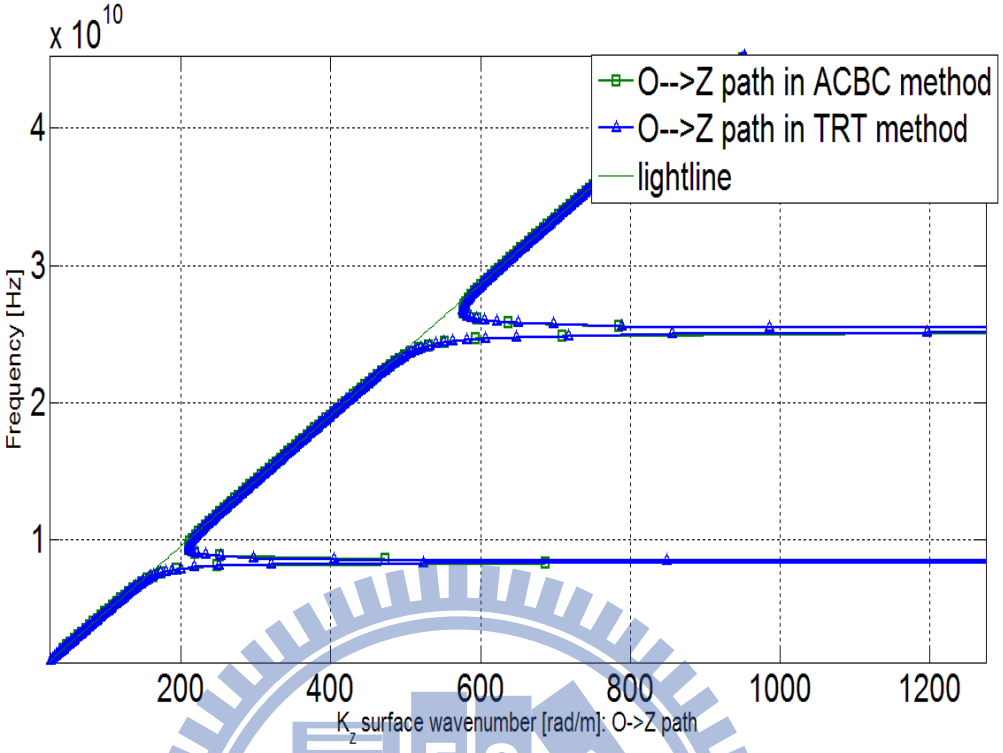

Figure 8(a): Comparison between the corrected ACBC method and TRT for O→Z path.

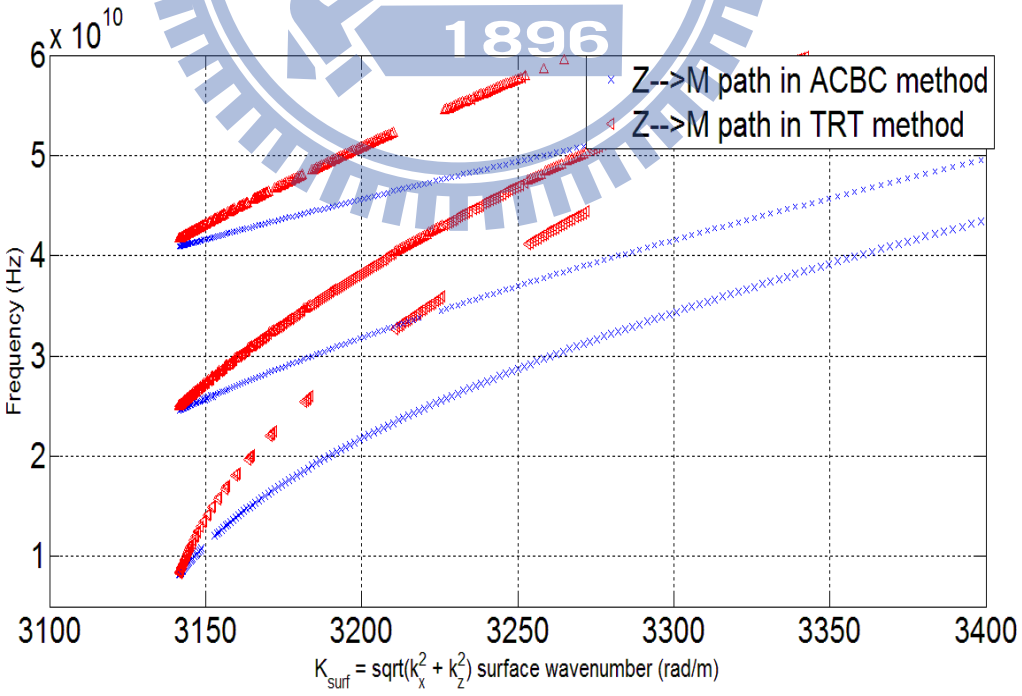

Figure 8(b): Comparison between the corrected ACBC method and TRT for Z→M path.

2-6 Field distributions

Fig. 9(a) and 9(b) show the variation of the magnitude of the *E*-field components against the vertical *y*-direction for various frequencies within the first surface wave passband (0 to 10GHz according to Fig. 5(a)), whereas the graphs of Figs. 10. are for the *H*-field components. As the frequency rises and moves deeper into the first surface-wave regime (2.05 through 9.05 GHz in 1GHz steps, as selected for plotting), the corresponding increased surface-wave phase constant k_z^{univ} beyond $k_{above} = \omega\sqrt{\mu_{abv}\varepsilon_{abv}}$ and thus strengthened attenuation constant α_y^{above} along the vertical *y* direction is indeed demonstrated by the progressively steepened exponential decay of the various field components with increasing frequency. In addition, the continuity of the $|E_z|$, $|H_x|$ and $|H_y|$ components across the $y = d$ interface between the corrugations and the upper half region is observed as required.

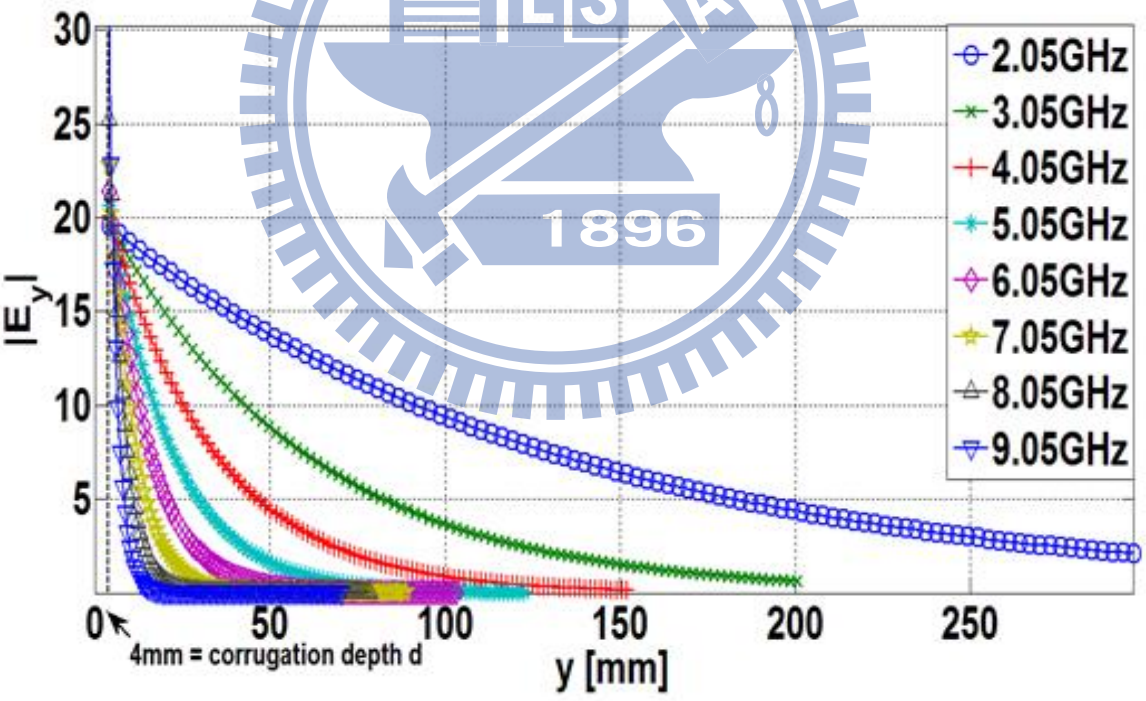

Figure 9(a): $|E_y|$ plotted against y-direction

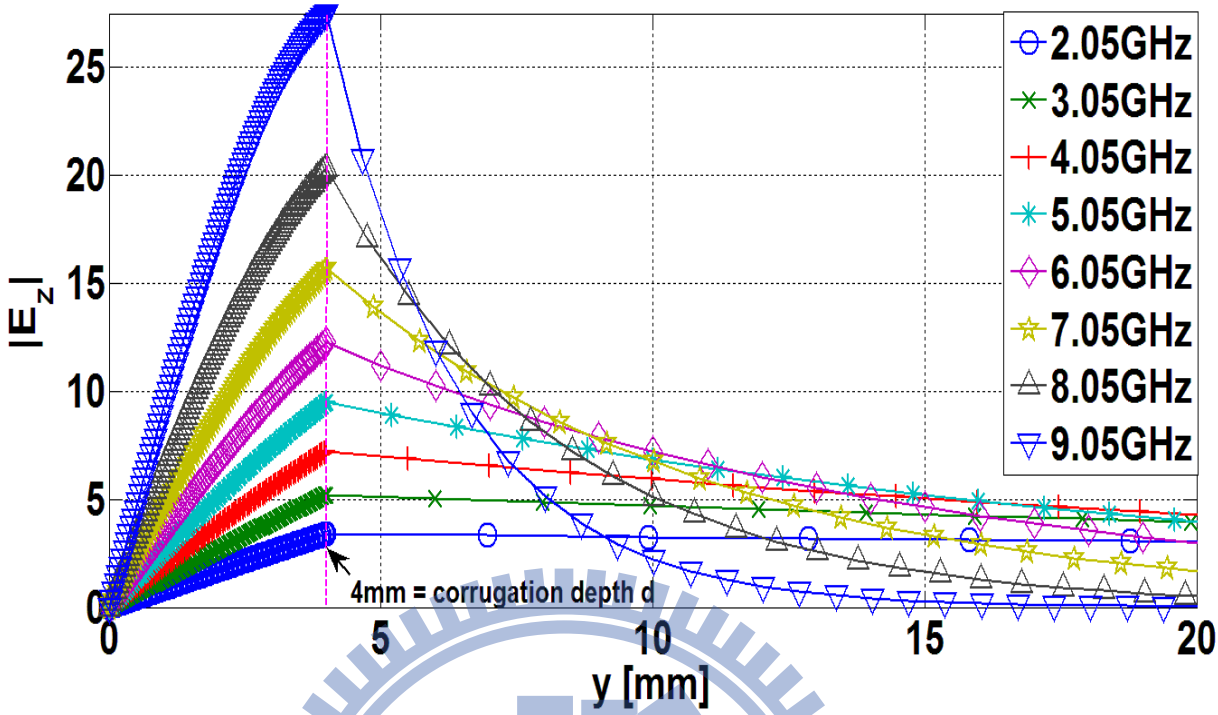

Figure 9(b): $|E_z|$ plotted against y-direction

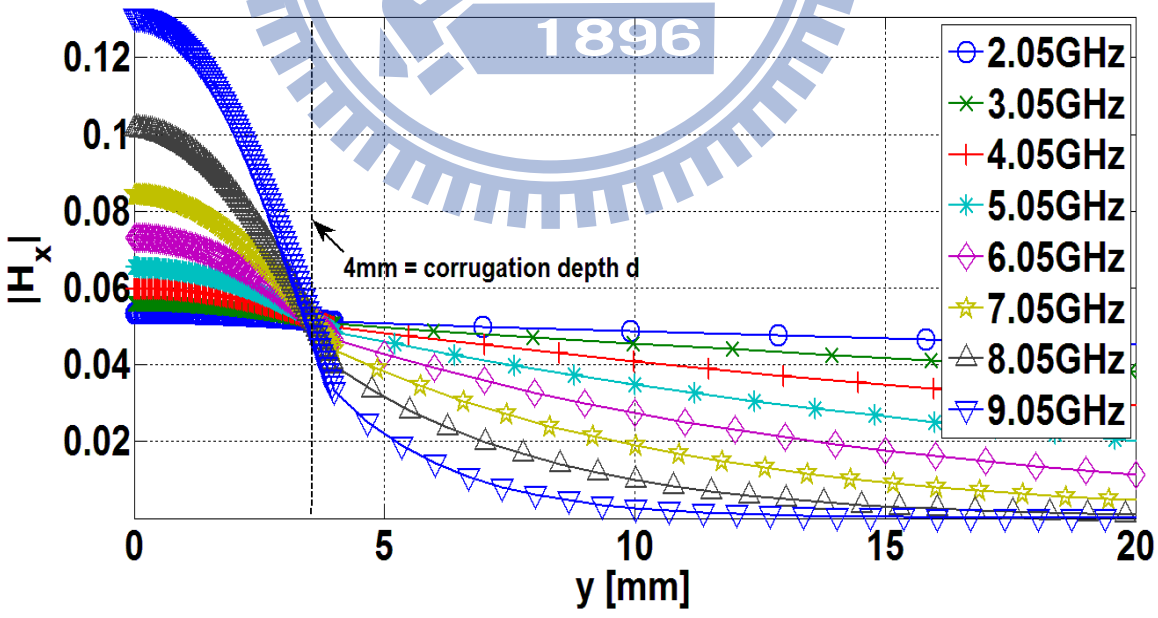

Figure 10(a): $|H_x|$ plotted against y-direction

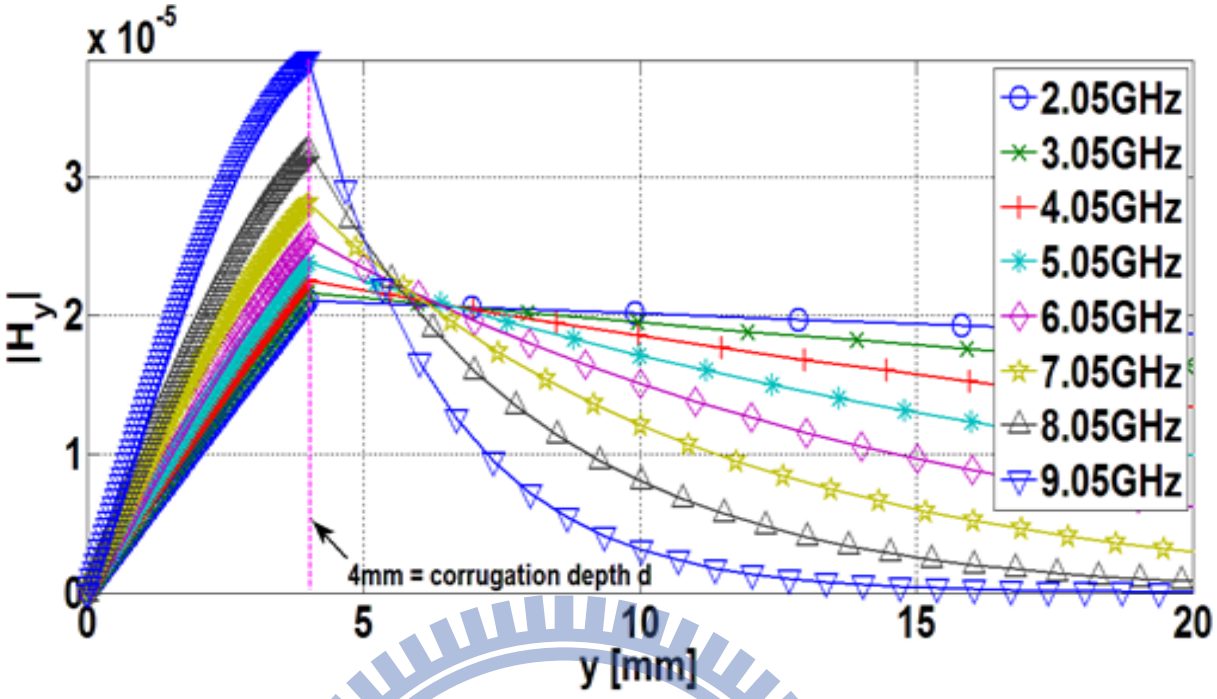

Figure 10(b): $|H_y|$ plotted against y-direction

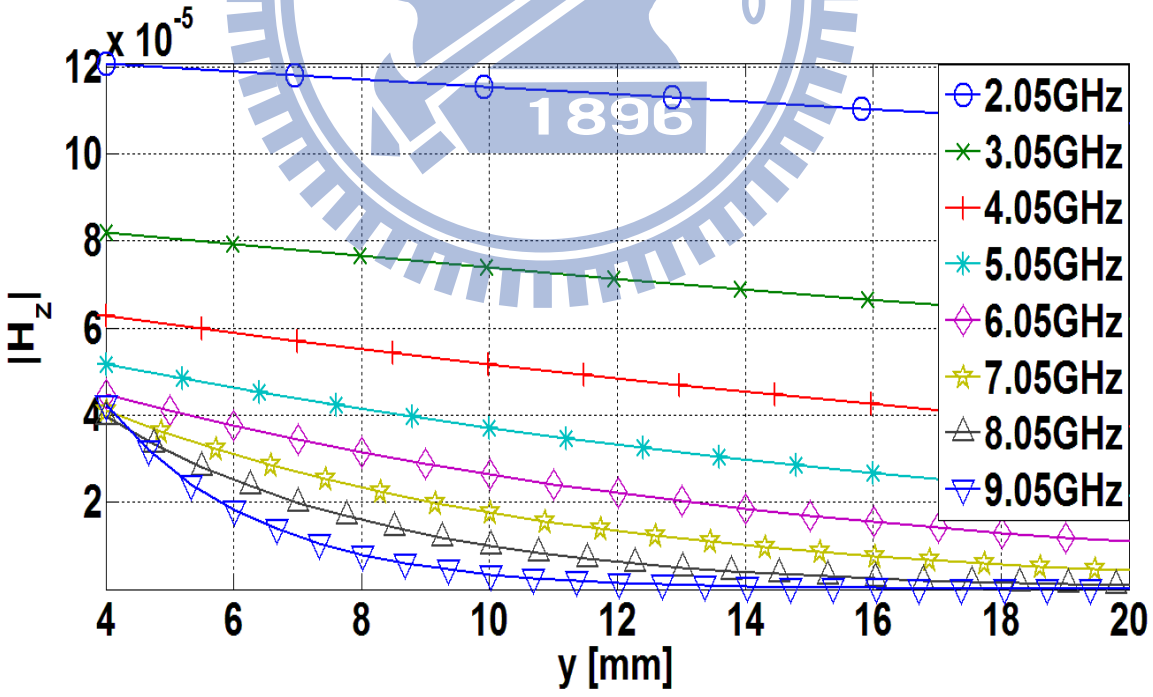

Figure 10(c): $|H_z|$ plotted against y-direction

III. Sectorial band gap

3-1 Dispersion diagram corresponding to Brillouin zone

For most of the studies in the literature, the EBG structures usually are used to deal with the entire bandgap, i.e. within the certain frequency bands, the surface waves are all suppressed on the EBG surfaces. There are potentially some applications which do not need a bandgap for all directions but just certain directions. Despite not potentially able to provide entire bandgap, planar corrugated surfaces are classically known to possess the capacity of offering surface-wave pass-bands and stop-bands along the directions parallel and perpendicular to the grooves and ridges, respectively, which are known as hard and soft surfaces as mentioned. However, no works have yet studied their candidature for serving as sectorial bandgap structures. We will demonstrate that planar corrugations are able to exude this capability. By capitalizing on the rapid surface-wave solution provided by the ACBC, we shall use the planar corrugated surface as the vehicle to illustrate how sectorial bandgap structures can be designed efficiently. This is something which no other periodic structures without analytic surface-wave solutions can readily afford.

Before we demonstrate the idea of sectorial band-gap and band-pass, we need to introduce the basis of the dispersion diagram and Brillouin zone. Brillouin zone is the set of

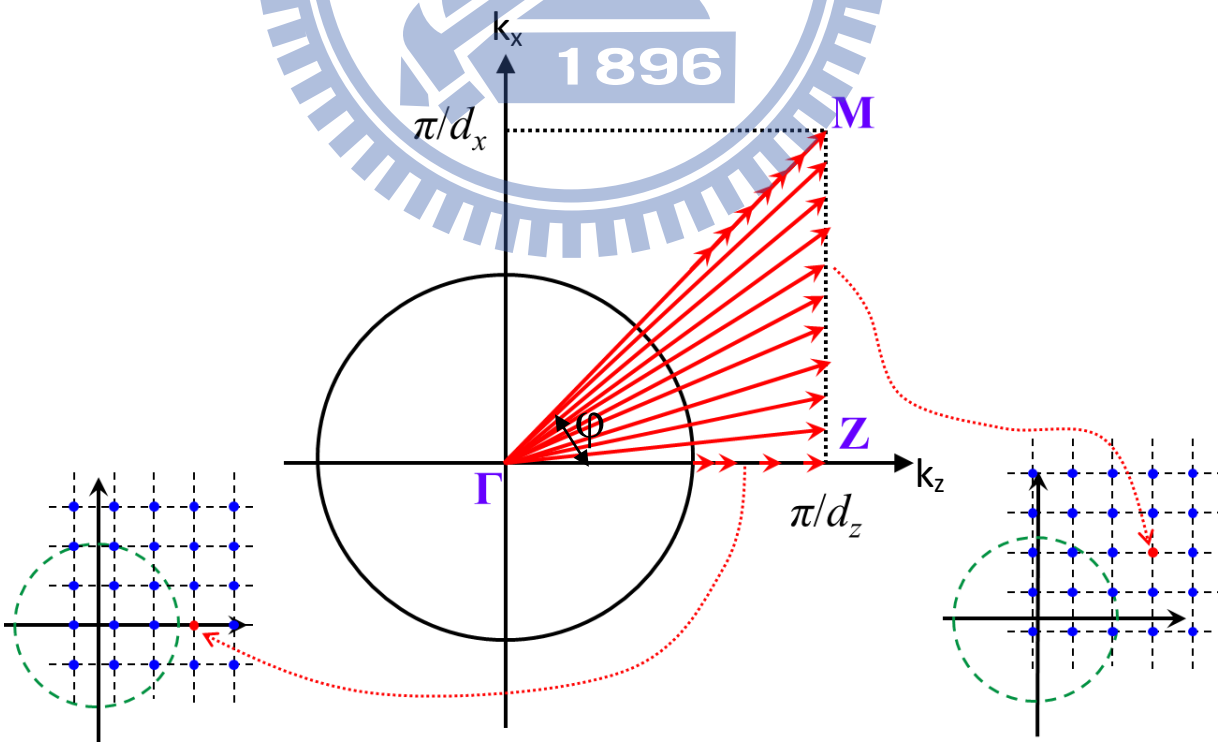

Figure 11: Brillouin zone

wavenumbers which can describe the propagation of electromagnetic waves in two-dimension photonic crystals, as shown in Fig.11, where k_0 is the wavenumber in free space. Since we only consider the surface wave, the wavenumber which is vertical to the corrugation must be pure imaginary, which leads to

$$k_{surface} = \sqrt{k_x^2 + k_z^2} \geq k_0 \tag{40}$$

so we just need to consider the region outside the circle for the surface wave case. As shown in Fig 11, each arrow constitutes a certain surface wavenumber for a certain frequency, but for the most important aspect here, there is not just only one surface-wave vector-arrow for any one certain frequency. This will be discussed deeper later.

In Section II, we show four parts (O→Z, Z→M, M→X, and X→O) of the dispersion diagram. As mentioned, any one of these parts is obtained by fixing two of these three unknowns, (i) k_x, (ii) k_z and (iii) frequency, and then the roots for the remaining unknown are solved for. If we set k_x as an unknown, and set

$$k_x = k_z \tan(\varphi) \tag{41}$$

where φ is the angle between the propagation path of the surface wave and the z axis. Then

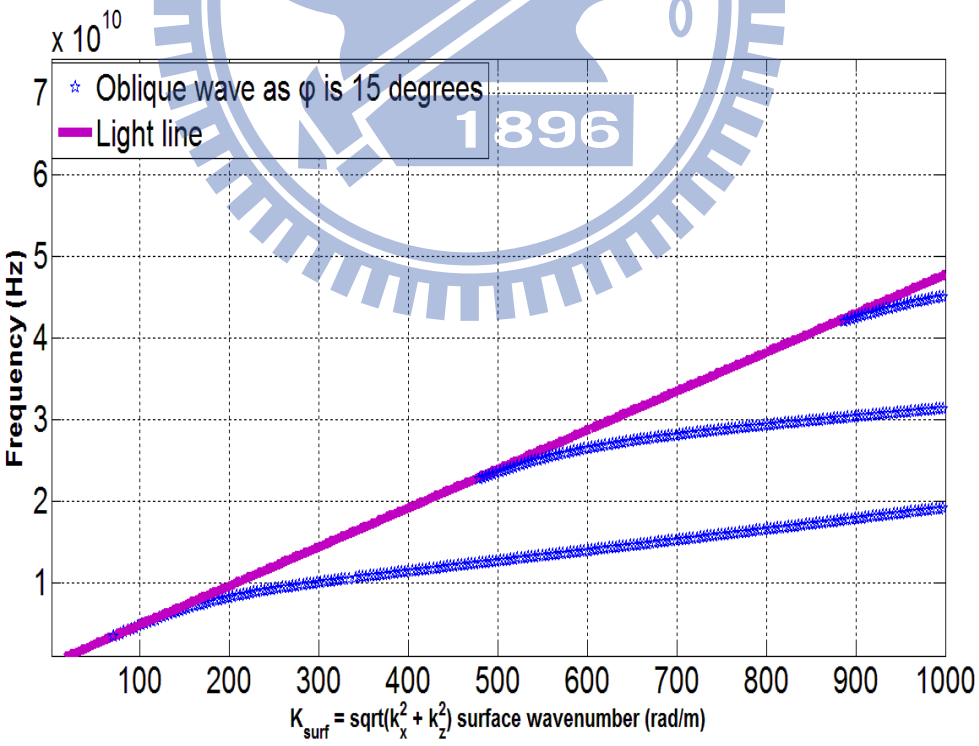

Figure 12(a): Dispersion diagram for oblique wave as φ is 15 degrees

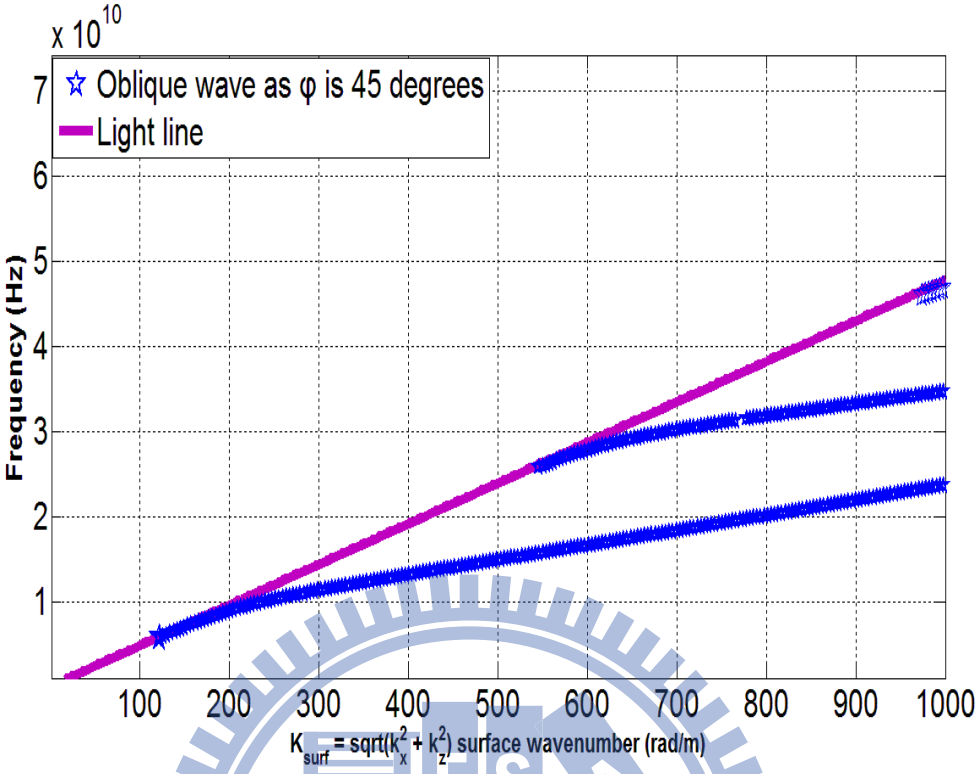

Figure 12(b): Dispersion diagram for oblique wave as φ is 45 degrees

the roots for k_z are solved we can get the dispersion diagram for the surface waves propagating along the path which has φ degrees with the z-axis. For the extreme case, we can take the X→O part as the 90 degrees cases turning from O→Z part. Two arbitrary different examples are shown in Fig. 12, the dimensions are as follows: d_z = 3mm, d=4mm, $\varepsilon_{rel,groove}$ = 3 and the values of φ are 10 and 45 degrees, respectively.

3-2 Concept of sectorial bandgap

Refer to the fictitious dispersion diagram in Fig. 13 below, which shows traces for various azimuth ϕ (measured from the *z*-axis perpendicular to the corrugations) directions of surface-wave modal propagation, i.e. each trace pertaining to a certain fixed ϕ, with the original dispersion paths of O→Z, Z→*beyond* included for reference. Let the frequency corresponding to the Brillouin limit be denoted as f_1. The associated surface-wavevector at this frequency is shown by the arrow in Fig. 14 with magnitude $k_{surf}{}^{f1} = \pi/d_z$ and directed along *z* perpendicular to the corrugations. As the surface-wavevector enters the oblique nonzero ϕ regime (ϕ measured from the *z*-axis perpendicular to the corrugations), but with k_z maintained at π/d_z, i.e. now the surface-wavevector component along *z* (k_z) is no longer zero,

both the eigen-frequency and modal surface-wavenumber increases further, the relationship between them as indicated by the traces corresponding to k_{surf} values greater than $k_{surf}^{f1} = \pi/d_z$. For illustration, the surface wavevector at an example frequency of f_2 (labeled in Fig. 13) is represented in Fig. 14 by the arrow with magnitude k_{surf}^{f2}. Due to symmetry about both horizontal and vertical axes, two arrows with magnitude k_{surf}^{f2} are shown in Fig. 14 (the same applies for other oblique surface-wavevectors). As the frequency rises further up to the point where the next higher-order surface-wave mode starts to emerge at f_3 as shown in Fig. 13, the surface-wavevector is directed towards an even larger ϕ angle as represented by the arrow with magnitude k_{surf}^{f3} in Fig. 14.

As it can be seen in Fig.13, the original stopband region for zero angular span (phi=0) is between f_1 and f_3, and for the case when phi is "φ_b" degrees, the stopband zone is from f_2 to f_3, so it means as the phi gets larger, the stopband areas get smaller. In other words, we can say that during the period from f_2 to f_3, there is "at least" "φ_b" degrees sectorial band gap area. It is easily misunderstanding the above idea in another expression which is Brillouin zone as shown in Fig.14. The sectorial bandgap angle (ϕ_{SBGA}, in degrees) is between f1 and f2, but not between f2 and f3. Also by applying the above idea, we can define the boundary between the conventional soft and hard surfaces, which is the surface-wavevector k_{surf}^{f3} in Fig.14, i.e. the sectorial bandgap angle corresponding to the frequency which the next mode just appears.

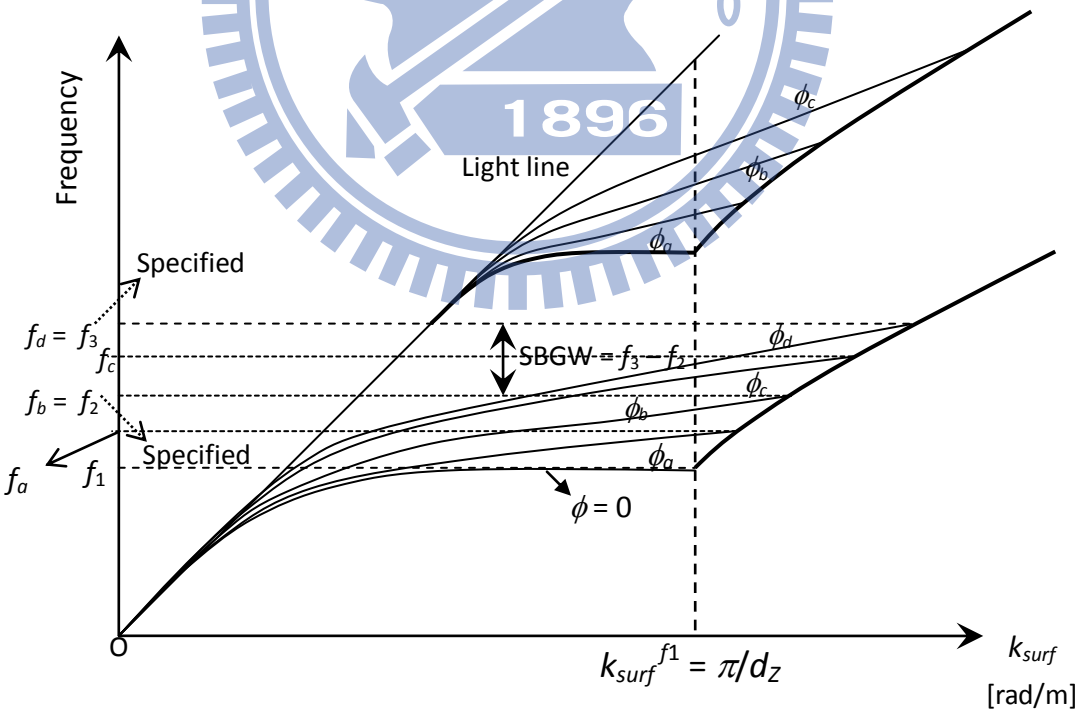

Figure 13: Fictitious dispersion diagram

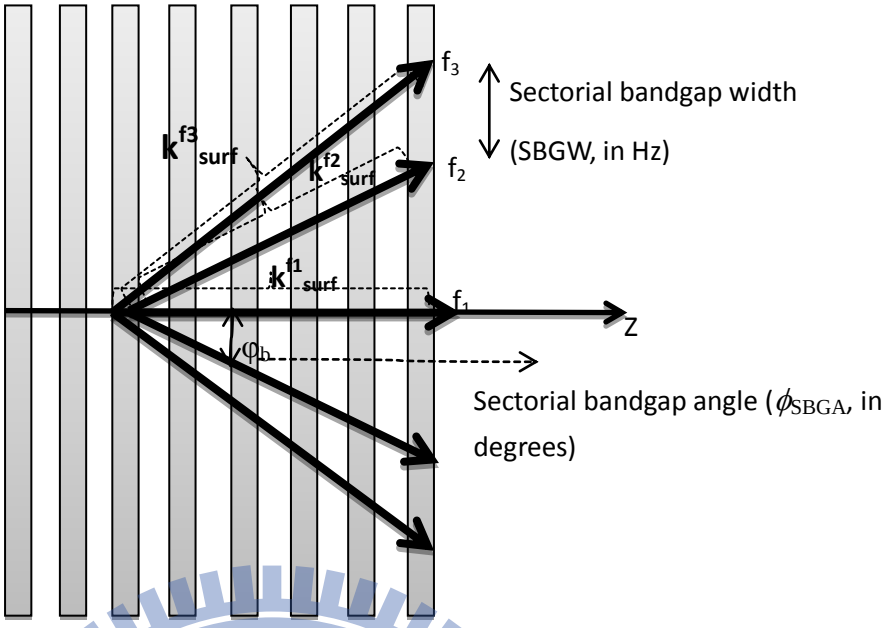

Figure 14: Top view schematic of corrugation

As mentioned, between frequencies f_2 and f_3, no surface wave can propagate within the sector between the two symmetric arrows with k^{f2}_{surf} (each being the surface-wavevector at f_2). We call the range between the f_2 and f_3 as sectorial bandgap width (SBGW=f_3-f_2, indicated in Fig.14), which means in this area, no surface-waves can propagate within the angular size with at least "ϕ_{SBGA} (which is φ_b in this case)" degrees. But why is the SBGW upper-limited by f_3? As the frequency just exceeds this frequency, the next higher-order surface-wave mode starts to appear and propagate along the *x*-direction. This of course falls inside the sector and thus disqualifies frequencies above f_3 from being included in the SBGW.

3-3 Sectorial bandgap corrugations design

The theory of the sectorial bandgap had been introduced in the previous section, and it will be convenient if the relationship between the dimension of the corrugation and the sectorial bandgap angle is known. For example, if the height of the corrugation is known, and also the target frequency is given, it is possible to provide relationship between the groove material and the sectorial bandgap angle it can reach. The idea can be done by using the Eq. (31) again. Substituting Eq. (31) by Eq. (41), setting the k_z as Brillouin limit and an arbitrary frequency, so the relative permittivity of the groove can be solved as the roots.

The dimensions of the corrugation in this example are as following: d = 4mm, d_z=2mm,

and g=1.6mm. Figure 15 shows O→Z path of dispersion diagram obtained by corrected ACBC method as the relative permittivity is 4.2, and as it is shown, the first and second stopbands start (which also means the initial point of the Z→M path) from 9GHz and 27.5GHz, respectively. Figures 16 show the relationship between the groove material and the sectorial bandgap angle, and three different frequencies are discussed here, which are 9GHz, 15GHz, and 27.5GHz. As shown in Fig. 16(a), there are two exponential curves which represent the first and second mode. Just as mentioned, 9GHz is the start of the first stopband, and it is shown that the first point (solution) of the first mode starts when the relative permittivity is 4.2, which corresponds to the initial condition. For the case as the frequency changes to 15GHz in Fig. 16(b), it is shown that both curves (modes) will move down, which means that the sectorial bandgap angle gets larger compared to Fig 16.(a) for the first mode. As the frequency becomes 27.5 GHz, which is the start point of the second stopband, there are two roots when the relative permittivity is 4.2, as shown in Fig. 16(c). One thing should be mentioned here, once the new mode enters the passband, even though there has solution for the first mode, the bandgap will be covered by the second mode, so that the phenomenon will not be seen. There is one thing should be

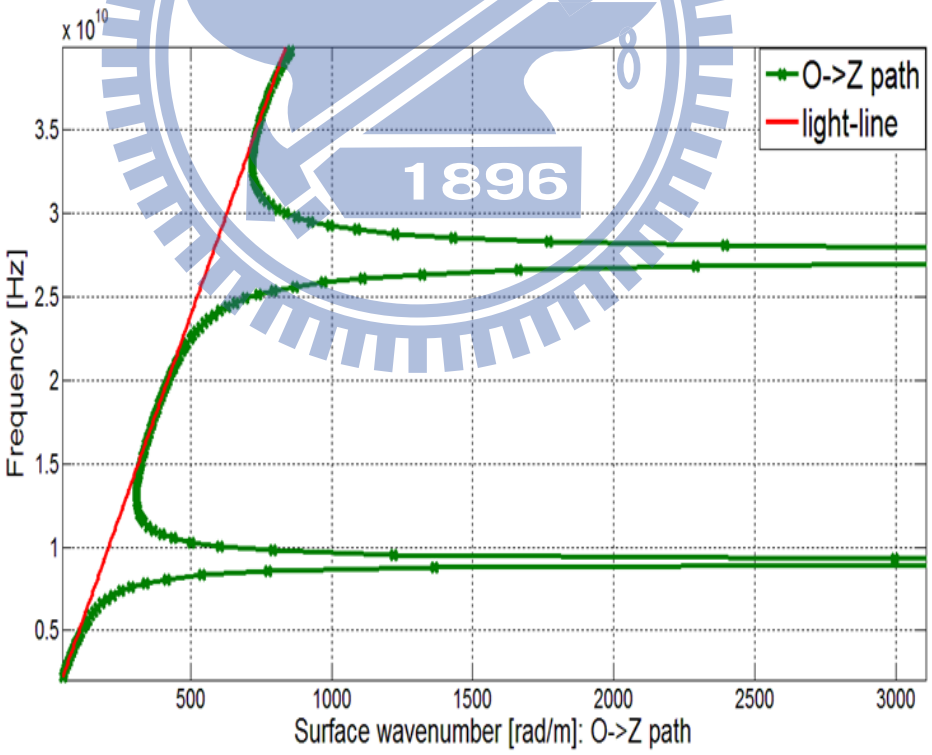

Figure 15: O→Z path of the dispersion diagram for present case

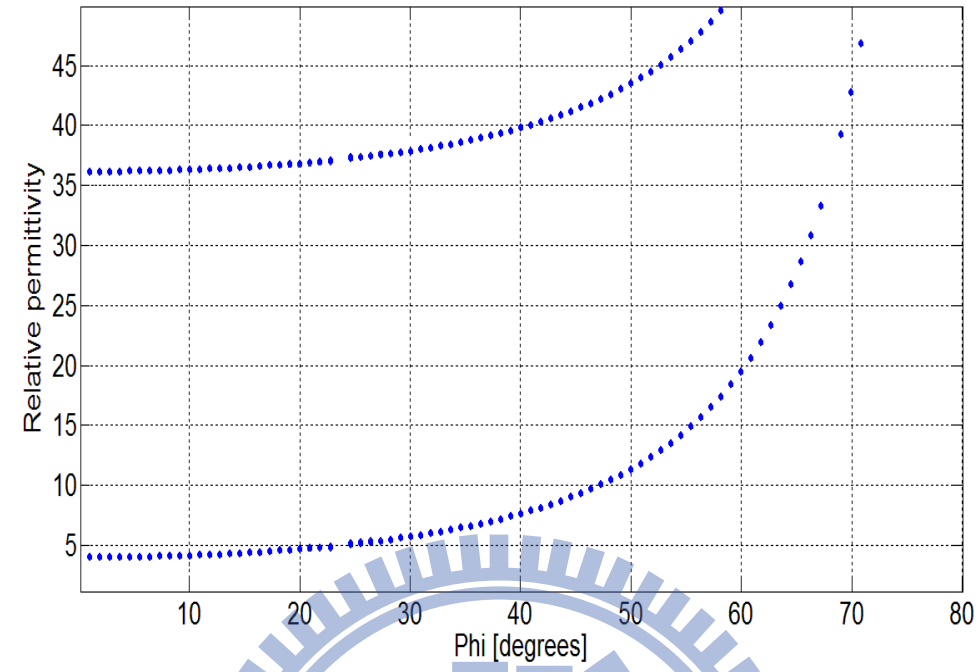

Figure 16(a): Relationship between relative permittivity and sectorial bandgap angle in 9GHz.

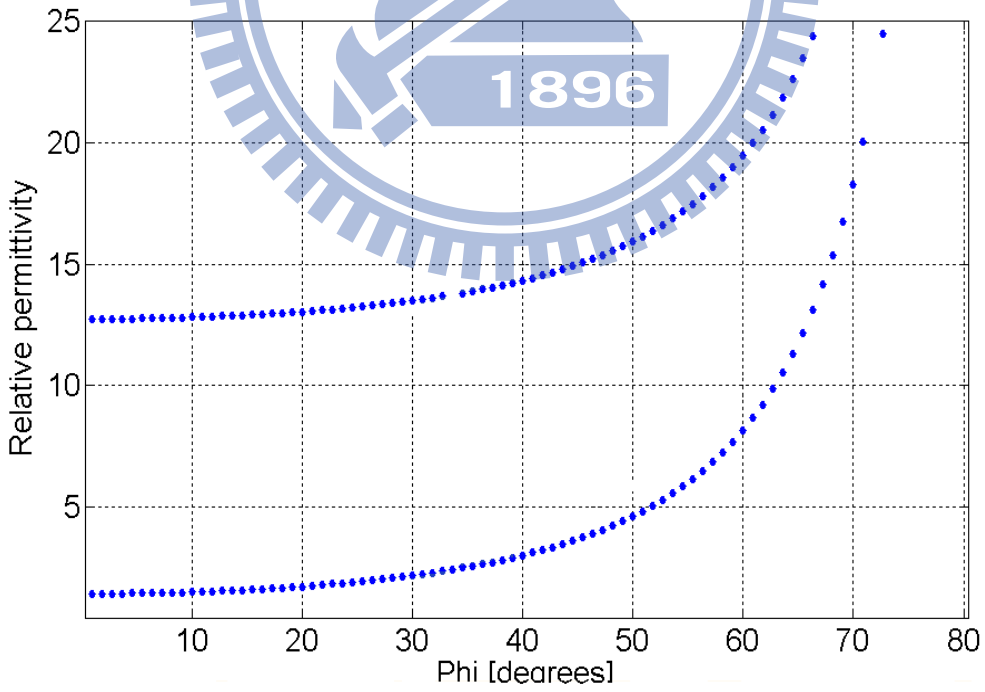

Figure 16(b): Relationship between relative permittivity and sectorial bandgap angle in 15GHz.

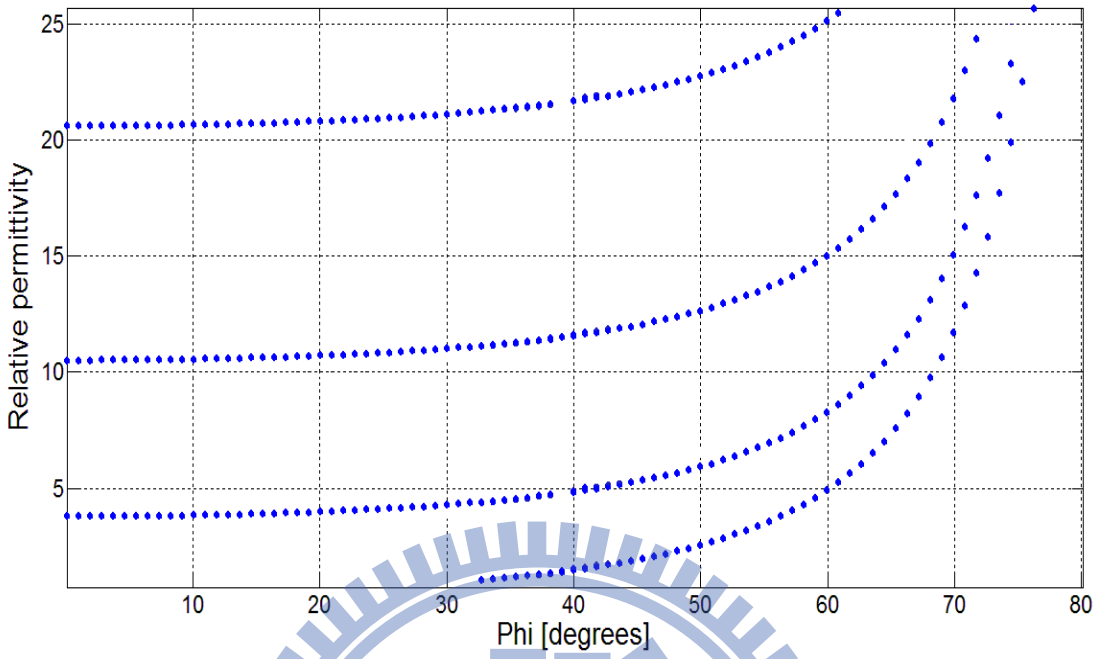

Figure 16(c): Relationship between relative permittivity and sectorial bandgap angle in 27.5GHz.

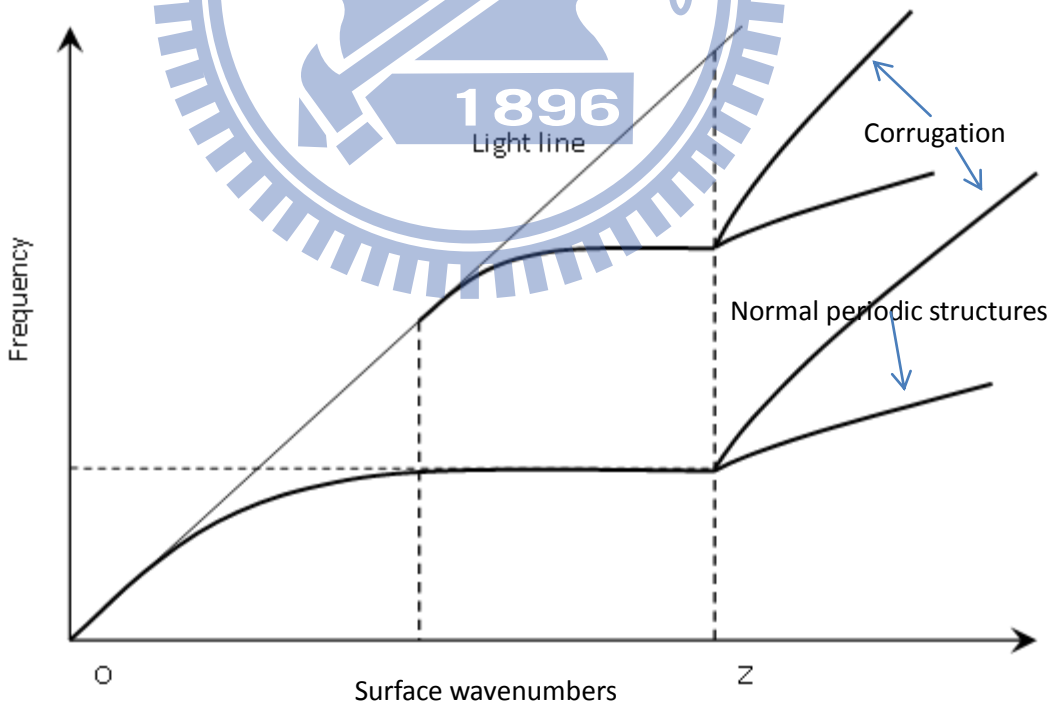

Figure 17: Comparison between corrugations and normal periodic structures

noticed that the predicted sectorial bandgap angle shown in Figs. 16 are ideal, which is because the loss tangent of the material in the grooves does not considered in ACBC method, so the results might have deviations, but the phenomenon still exist.

The same phenomenon may occur in other periodic structures, but the corrugation can achieve the best result. The reason is that we can notice that compared to the normal periodic structures, the slope of the Z→M part of the dispersion diagram for the corrugation is steep, as shown in Fig. 17. Since the slope is steep, the corrugation does not have "any direction" bandgap, but this special characteristics caused the corrugation achieve the sectorial bandgap idea. For the normal periodic structures whose slopes are flat, the SBGW may be too small to clarify which cause the difficulty to reach the idea.

3-4 Simulation results

For the reality, it is difficult to get the dispersion diagram directly, and for most of the literature, the simplest way to explain the dispersion diagram will be the scattering parameters. In this section, the simulation results for the sectorial bandgap will be shown, and we use the transmission coefficient to verify the sectorial bandgap theory. The results are verified by CST software.

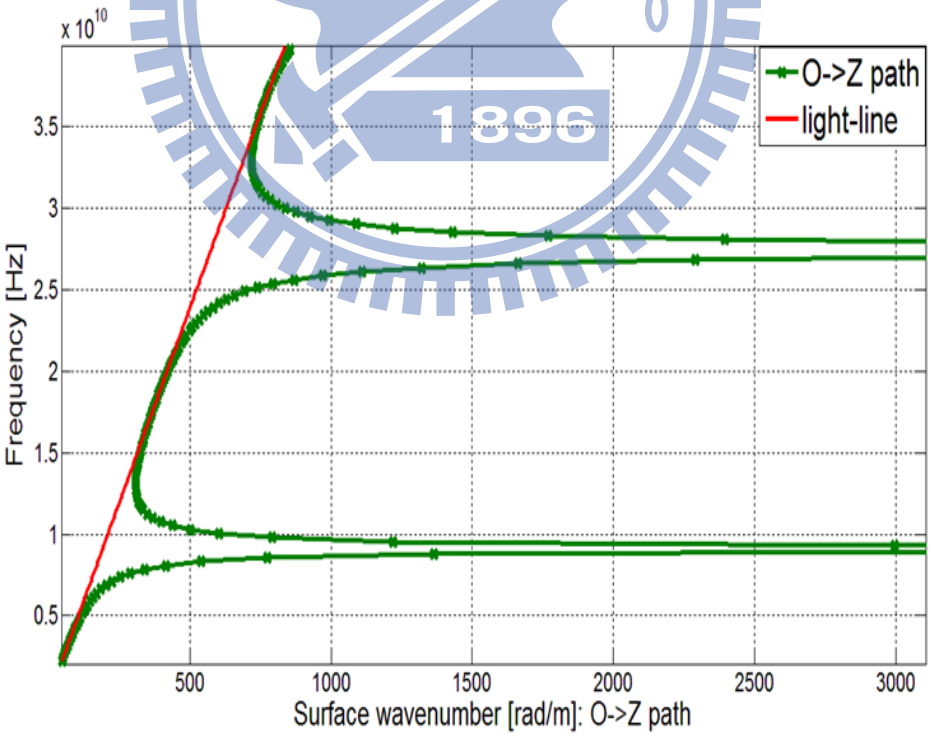

Figure 18(a): O→Z part of the dispersion diagram as the material of the groove is FR4.

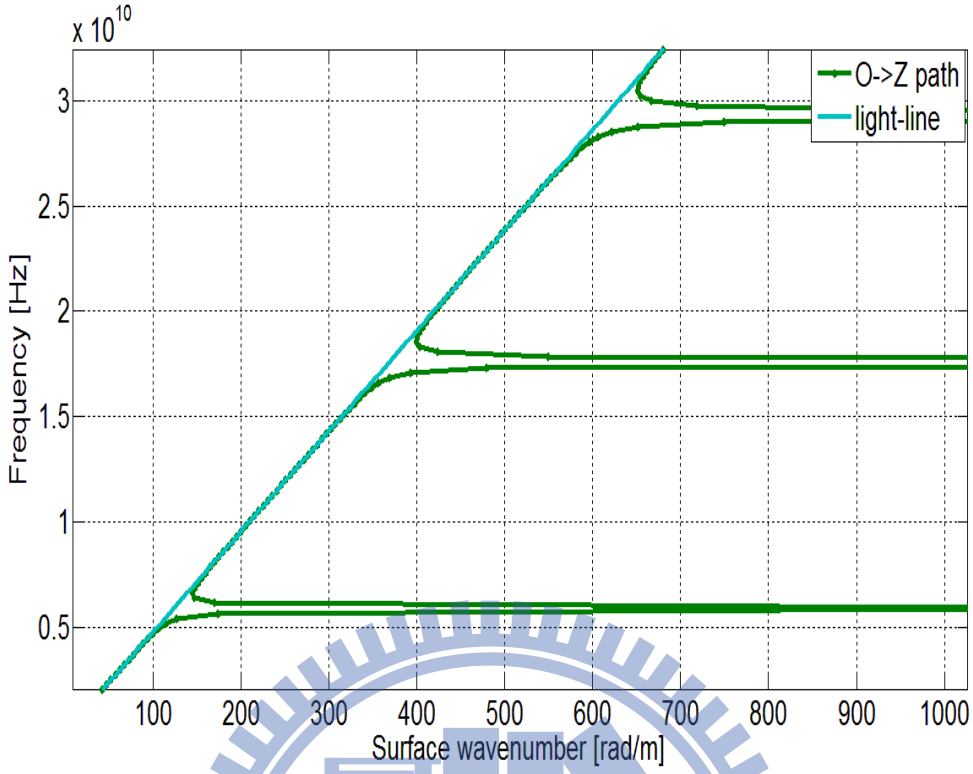

Figure 18(b): O→Z part of the dispersion diagram as the material of the groove is Rogers RT6100.

In this section, the dimensions we choose are as following: d = 4mm, d_z=2.6mm, and g=1.6mm, also we examine two different cases, for which the material we choose are FR4 and Rogers RT6010, whose relative permittivity is 4.2 and 10.2 respectively. At first, the O→Z part of the dispersion diagram obtained by the ACBC methods for above mentioned dimensions are shown in Figs. 18. The start frequencies of the stopband in Fig. 18(a) are 8.8GHz and 26GHz, and about 17GHz and 29GHz in Fig. 18(b). Figs. 19 show the top view of the corrugation in CST simulations, and we use the two identical waveguides as sources and receivers (the cutoff frequency for the waveguides is 1.53GHz), since the limitation in CST setting, for verifying the oblique waves on corrugation surface, we rotate the corrugation for 30 degrees meanwhile fixing the distance of the waveguides. The transmission coefficients for two different cases are shown in Figs. 20, which represent the relative permittivity as 4.2 and 10.2, respectively. By observing the 0 degree in Fig 20(a), it can be seen that stopband bandwidth is wider than the prediction as shown in Fig 20(a). The reason is just as mentioned that it is because that in ACBC method, loss tangent of the material in the grooves is not considered, so that when dealing with the practical cases, some surface waves may decay in the grooves. For the material such as Rogers RT6010, the value of loss tangent is much smaller than FR4, so the simulation error compared to ACBC methods is also smaller, which is shown in Fig. 20(b). In Figs. 20, the transmission coefficients of oblique waves for 30

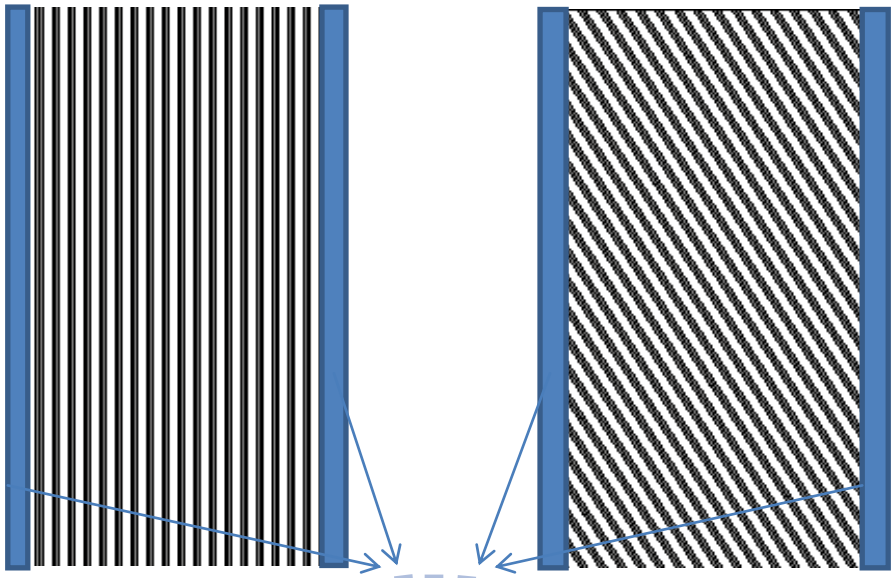

Figure 19: Top view of the corrugation in (a) 0 and (b) 30 degrees rotation in CST simulations.

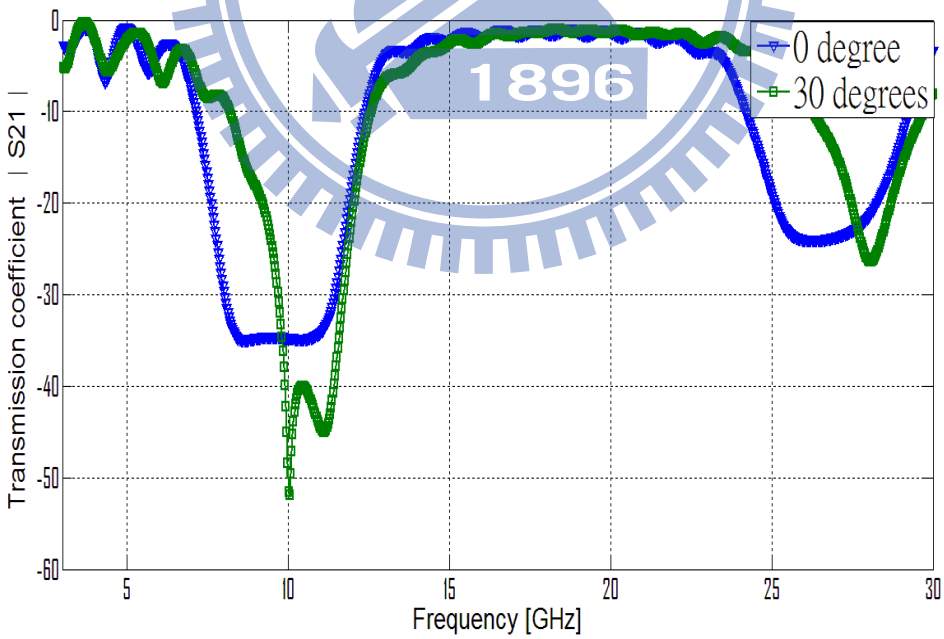

Figure 20 (a): Transmission coefficient results using FR4 as the material of the grooves.

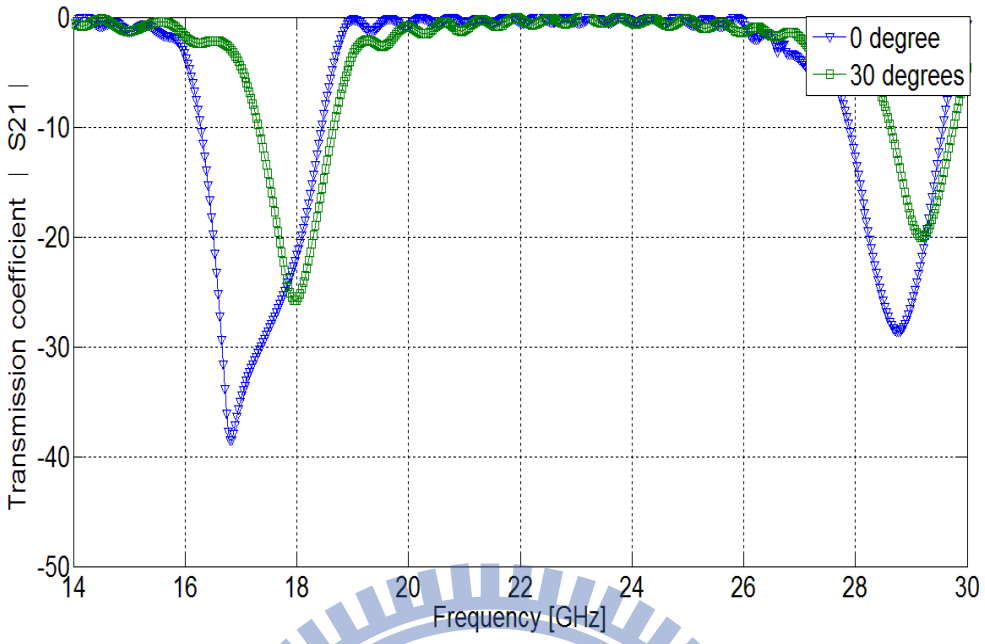

Figure 20 (b): Transmission coefficient results using Rogers RT6010 as the material of the grooves.

degrees are also simulated. Just as presumed, the stopband bandwidth gets smaller as the angle decreases. Take Fig 20(a) as example, 7.5GHz is f_1 as the symbol in Fig. 14, 9 GHz is f_2, and 12GHz is f_3. So during 9GHz to 12GHz, we can get "at least" 30 degrees sectorial bandgap angle, and the SBGW is 3GHz (which is due to 12GHz-9GHz).

3-5 Measurement results

In this section, the measurement results will be shown. The dimensions of the corrugation we fabricate are as followings: d_z = 2mm, g=1.6mm, d = 4.5mm, and $\varepsilon_{rel,groove}$ = 4.3. The structure is shown in Figs. 21, and the dispersion diagram retrieved from ACBC method is in Fig.22. Two k-band (from 18GHz to 26.5GHz) horn antennas are used as the source and receiver, and they are put on the corrugation surface. Since the aperture of the horn antenna is tall from the surface, the absorbers are stuck on the apertures and just leave a thin gap in the bottom in order to be closer as a surface wave. In the beginning, two horn antennas are placed face to face, and theoretically, the energy is 100% through so that the value of S_{21} should be 0dB. But we want the wave to be more like a surface wave propagating on corrugation surface, the absorbers are added to block most areas of the aperture, so the energy is absorbed. The setting framework described above is shown in Fig. 23, and the section view is in Fig.24.As we can see in Fig. 25 that the reference is about -22dB. Then we put the corrugation under the

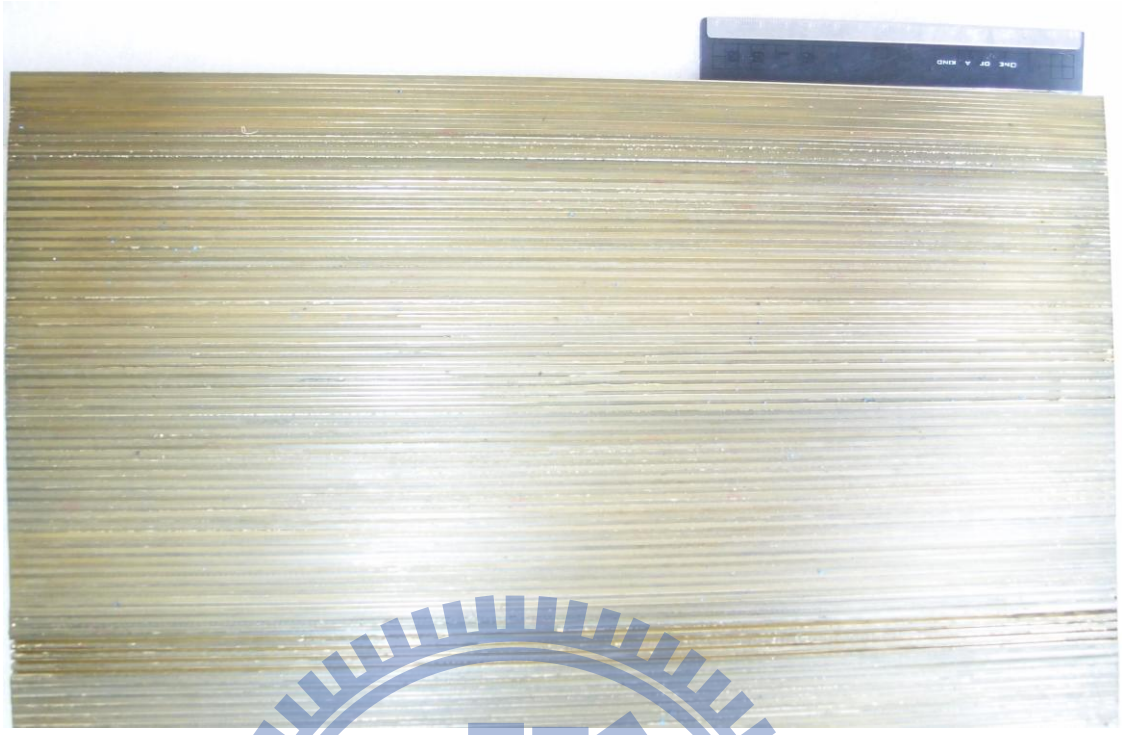

Figure 21(a): Top view of the fabricated corrugation

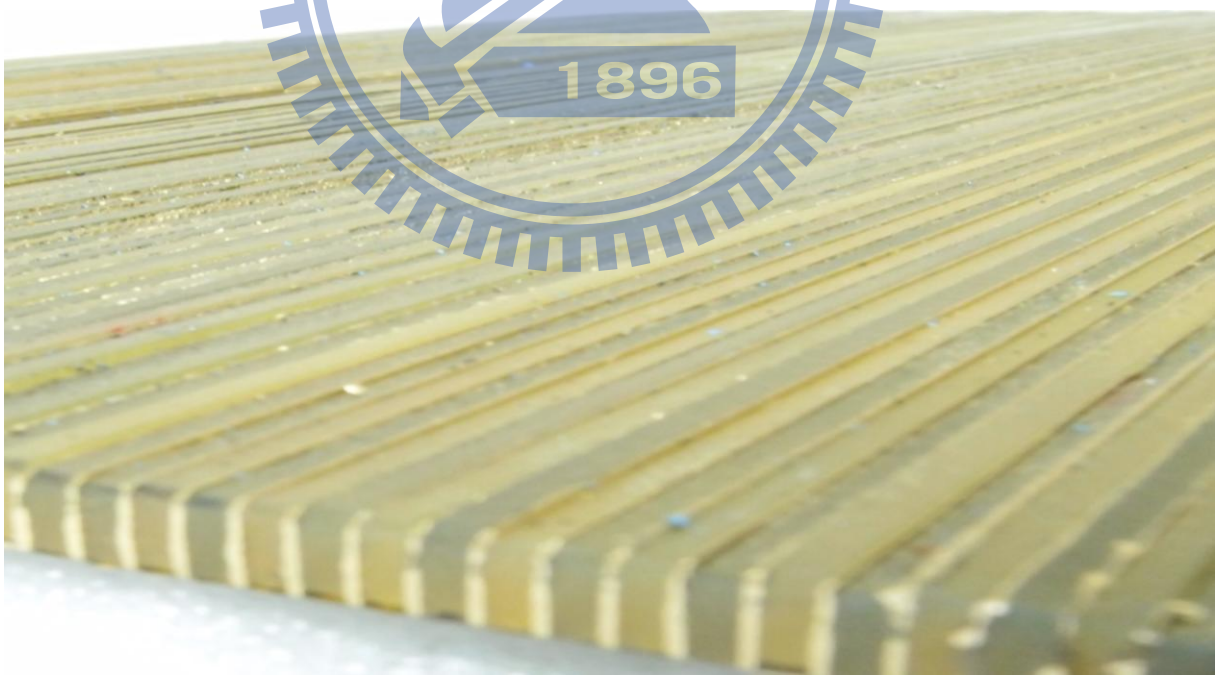

Figure 21(b): Side view of the fabricated corrugation

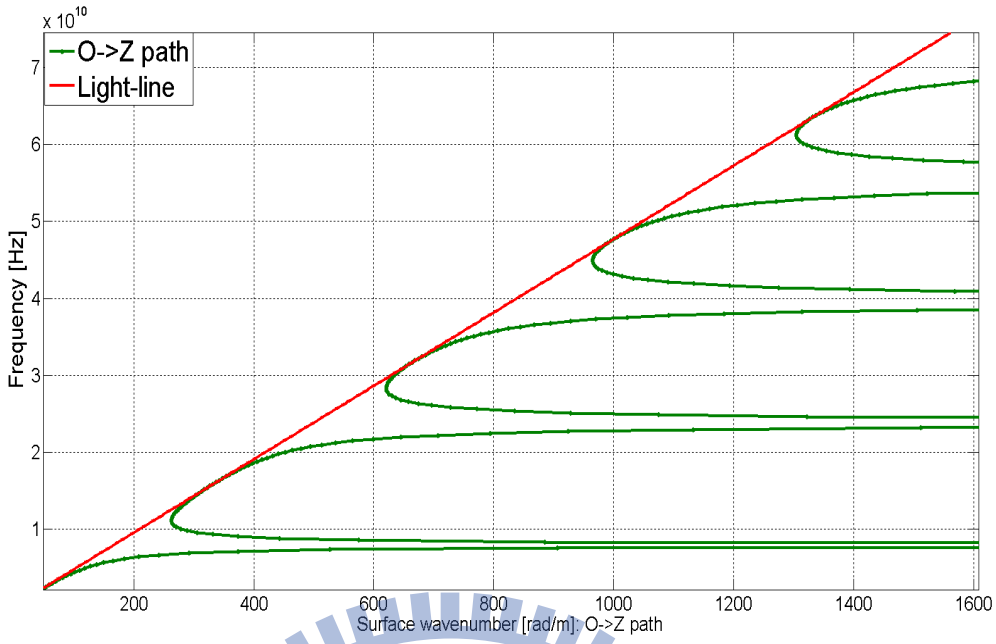

Figure 22: O→Z part of the dispersion diagram

Figure 23: Measurement framework.

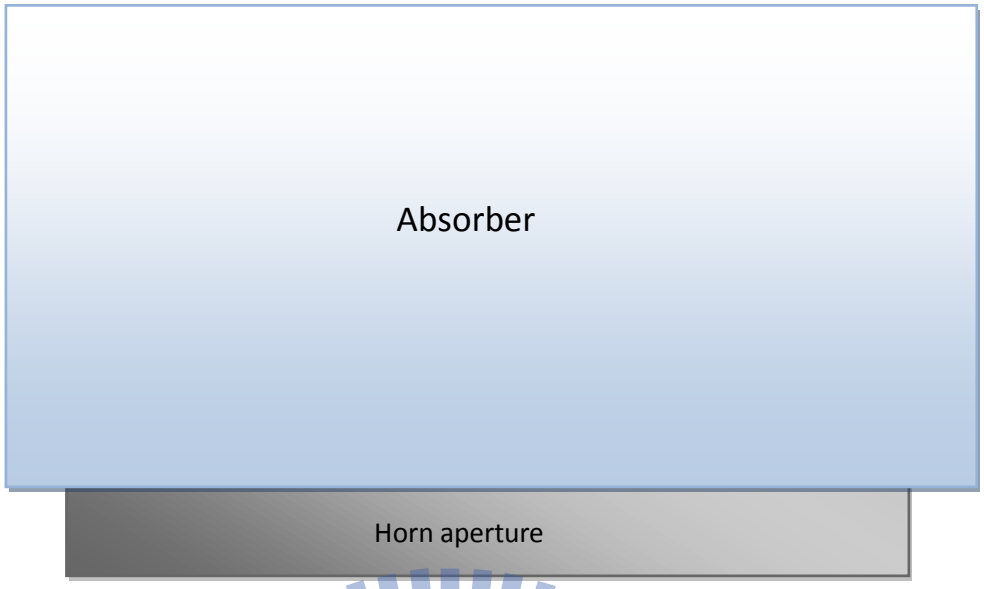

Figure 24: Section view

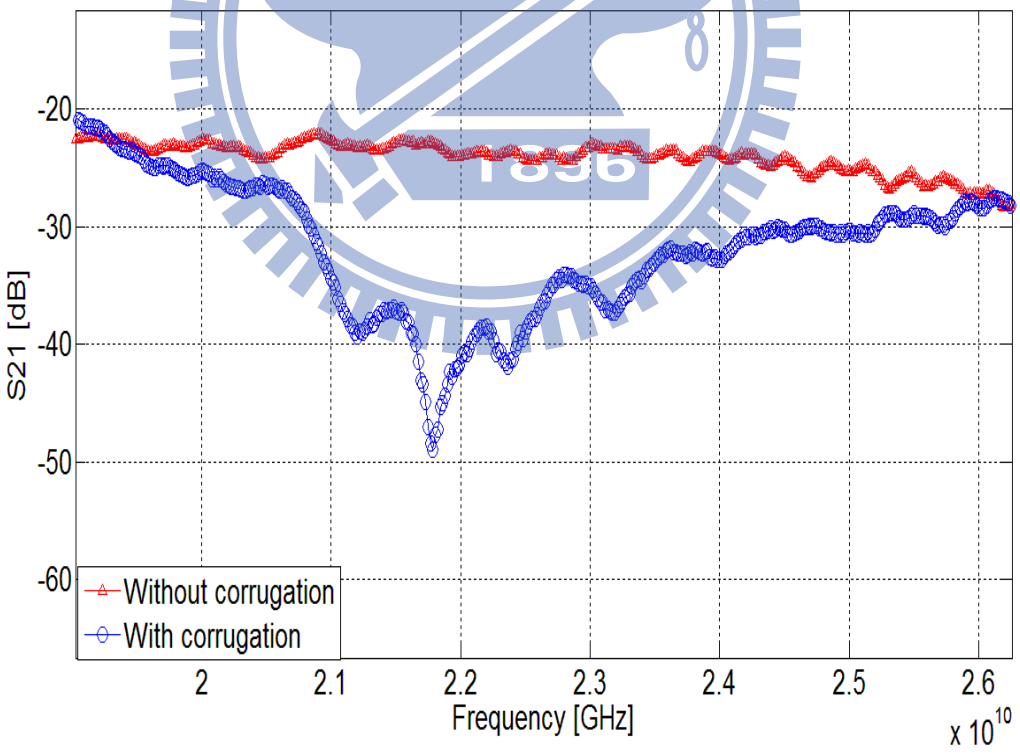

Figure 25: Measurement results for the existence of the corrugation.

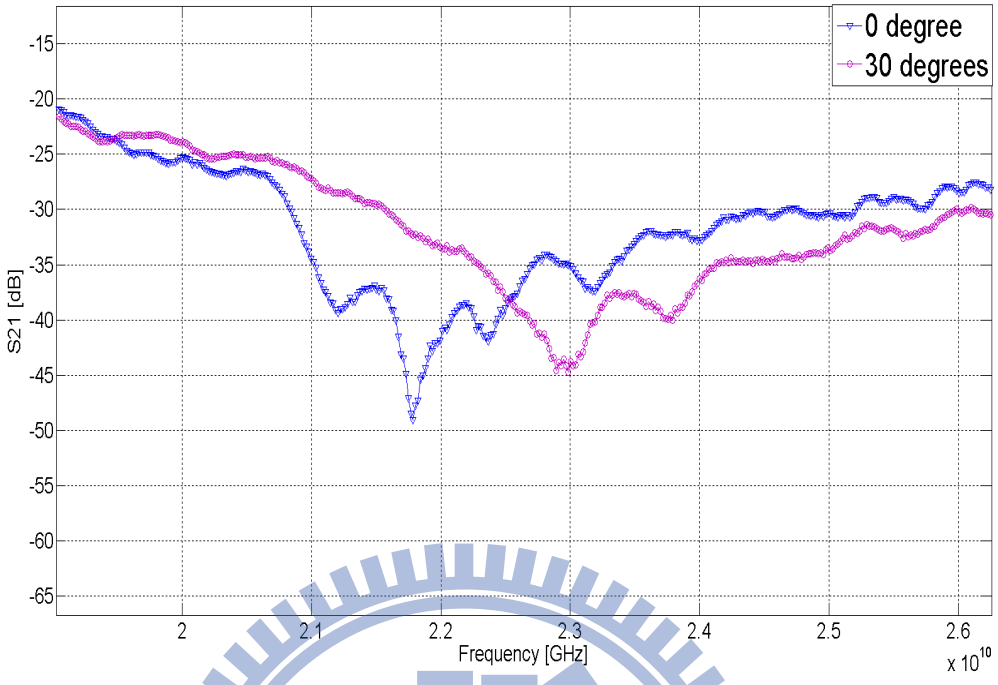

Figure 26: Comparison for the results as the corrugation rotates 0 degree and 30 degrees.

horns, and it can be observed that there exists a stopband region between 21GHz to 26GHz, for which this region is also the stopband area in dispersion diagram obtained from ACBC method as shown in Fig. 22. Figure 26 shows the comparison as the corrugation rotates 0 degree and 30 degrees. The trends are similar to the simulation results. The larger angles the corrugation rotates, the start frequency of the stopband will be higher, which means that the stopband bandwidth is smaller.

IV.Relationship between scattering parameters and dispersion diagram

4-1 Introduction

Most of the time, in order to obtain knowledge of just the width and location in the frequency spectrum of bandgaps of periodic structures, the use of two-port scattering parameters is more direct than the dispersion diagram. Nonetheless both approaches have their own benefits. Scattering parameters can characterize the center frequency, bandwidth, and the attenuation level of the stop band, while dispersion diagram can show the relationship between the frequency and wavenumber, further allowing the retrieval of data such as the phase velocity. For most research in the literature, dispersion diagrams are generated by full wave simulators, and when it comes to the measurement stage, the diagrams are difficult to gauge directly, so the scattering parameters are used to explain the dispersion diagram instead. But scattering parameters are after all only intermediate results, shedding no insights at all aboupt the wavenumber at that frequency. It will be more convenient if we could know the relationship between the scattering parameters and dispersion diagram, and then we could use the directly measurable S-parameters to generate the measured dispersion diagram.

For a normal periodic structure whose equivalent circuit is not complicated, it is easy to get the expression of the wavenumber by ABCD matrix, which will be briefly introduced later. But for a more complicated periodic structure, the equivalent circuit is complex, resulting in the difficulty to deal with the matrix in the previous method. Since the equivalent circuit is too complex to analyze, it is a good way to treat this complex unit cell as a uniform material. In other words, the scattering parameters are obtained at first, and then we reconsider the unit cell as a uniform material, deriving the relationship between the scattering parameters and wavenumbers, finally substituting the measured scattering parameters into the relationship. In this section, we will show the process of deriving based on a simple theory, and the accuracy for the transformed dispersion diagram is good.

In [16], Pozar analyzed a periodically loaded transmission line, and its equivalent circuit is shown in Fig.27, where d is the distance between two unit cells, and b is the value of susceptance. Since it can be seen as a cascade of identical two port networks, we can use ABCD matrix to relate the voltages and currents on either side of the unit cell:

$$\begin{bmatrix} V_n \\ I_n \end{bmatrix} = \begin{bmatrix} A & B \\ C & D \end{bmatrix} \begin{bmatrix} V_{n+1} \\ I_{n+1} \end{bmatrix} \tag{42}$$

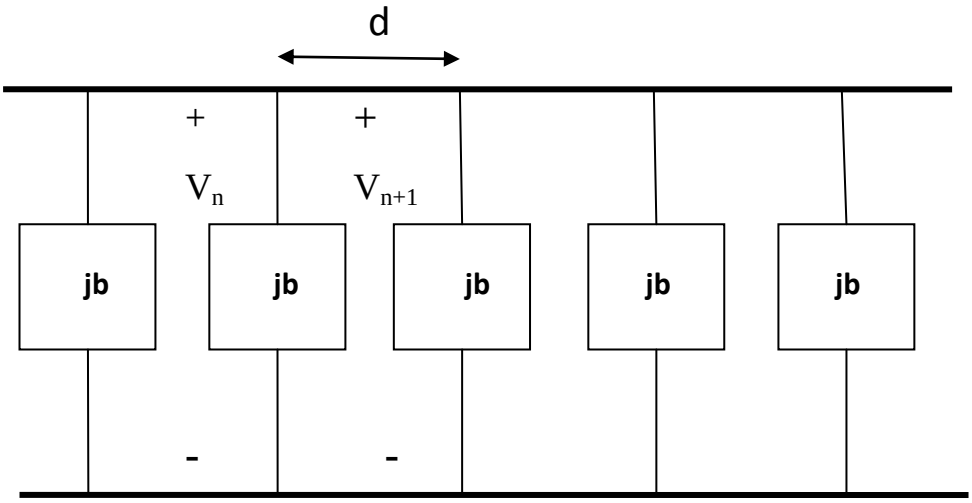

Figure 27: Equivalent circuit model of an infinite long periodically loaded transmission line.

where

$$\begin{bmatrix} A & B \\ C & D \end{bmatrix} = \begin{bmatrix} \cos\frac{\theta}{2} & j\sin\frac{\theta}{2} \\ j\sin\frac{\theta}{2} & \cos\frac{\theta}{2} \end{bmatrix} \begin{bmatrix} 1 & 0 \\ jb & 1 \end{bmatrix} \begin{bmatrix} \cos\frac{\theta}{2} & j\sin\frac{\theta}{2} \\ j\sin\frac{\theta}{2} & \cos\frac{\theta}{2} \end{bmatrix} \tag{43}$$

From Eq. (43), we can get

$$AD - BC = 1 \tag{44}$$

Now consider the phase difference between the nth and (n+1)th terminals

$$V_{n+1} = V_n \exp(-\Upsilon d) \tag{45.a}$$

$$I_{n+1} = I_n \exp(-\Upsilon d) \tag{45.b}$$

Substituting Eq. (45.a) and Eq. (45.b) into Eq. (42), we can get

$$\begin{bmatrix} A - e^{\Upsilon d} & B \\ C & D - e^{\Upsilon d} \end{bmatrix} \begin{bmatrix} V_{n+1} \\ I_{n+1} \end{bmatrix} = 0 \tag{46}$$

For nontrivial solutions, the determinant of the matrix in Eq. (46) must vanish, leading to

$$\cosh \Upsilon d = \frac{A+D}{2} \tag{47}$$

For a lossless periodic structure and symmetric network

$$\cos \beta d = A \tag{48}$$

Since we know the relationship between β and matrix element A in Eq. (48), and also the relationship between matrix element A and scattering parameters in two-port networks is already known, we can easily get the dispersion diagram if we have scattering parameters data.

4-2 Theory

The relationship between the scattering parameters and wavenumbers introduced by Pozar is only suitable for simple cases. For a more complex periodic structure, the equivalent circuit is not easy to retrieve. Even though the equivalent circuit can be retrieved, the susceptance would be too complicated, causing difficulties with the calculation using the abovementioned method. To solve this problem, we can think of it from another perspective, which is by treating the complex unit cell as a uniform material whose effective relative permittivity and permeability are ε_r and μ_r, respectively, as shown in Fig.28. The representations of the reflection and transmission coefficients are stated as follow:

$$\frac{V_{ref}}{V_{inc}} = \Gamma_{in} = S_{11} \tag{49}$$

$$\frac{V_{tra}}{V_{inc}} = T_{out} = S_{21} \tag{50}$$

Considering the multi-reflections in the material as shown in Fig 29, the total reflection coefficient in Eq. (49) can be represent as

$$\Gamma_{in} = \Gamma_{12} + T_{12}T_{21}\Gamma_{23}\exp(-2j\beta l) + T_{12}T_{21}\Gamma_{23}^2\Gamma_{21}\exp(-4j\beta l) + \ldots$$

$$= \Gamma_{12} + T_{12}T_{21}\Gamma_{23}\exp(-2j\beta l)\sum_{n=0}^{\infty}\Gamma_{23}^n\Gamma_{21}^n\exp(-2j\beta l) \tag{51}$$

Utilizing the formula of sum of the geometric series, which is

$$\sum_{n=0}^{\infty} x^n = \frac{1}{1-x} \tag{52}$$

we can represent Eq. (51) as

$$\Gamma_{in} = \Gamma_{12} + \frac{T_{12}T_{21}\Gamma_{23}\exp(-2j\beta l)}{1-\Gamma_{23}\Gamma_{21}\exp(-2j\beta l)} \tag{53}$$

Now we assume that both medium in the left-hand side and right-hand side of the material are air, resulting in

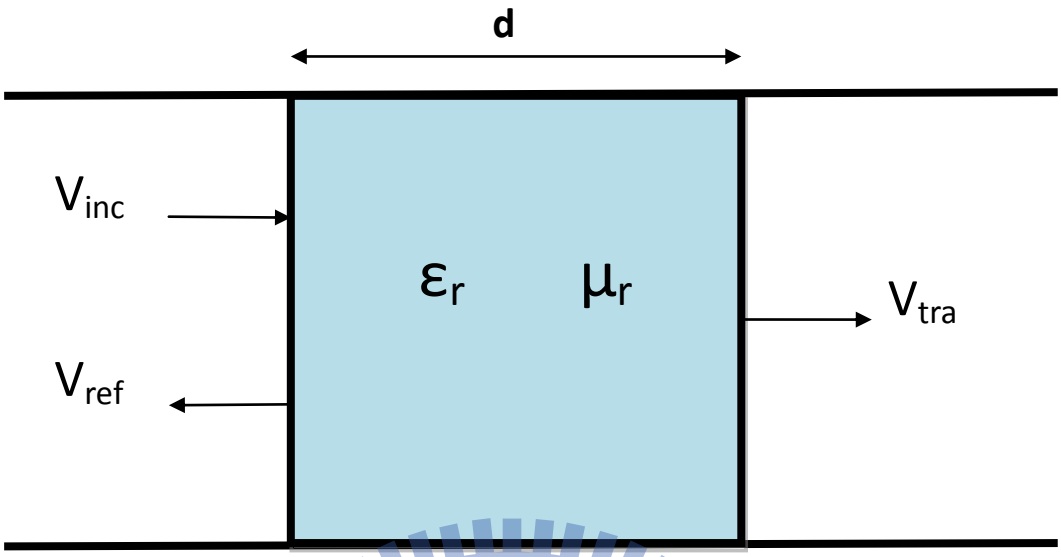

Figure 28: Two port network

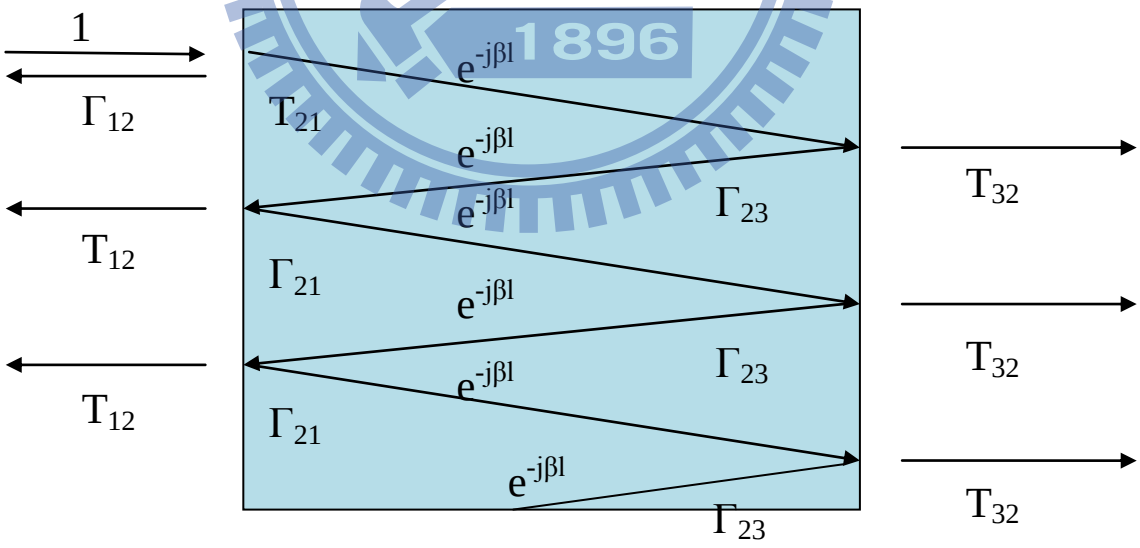

Figure 29: Multi-reflections in the material

$$\Gamma_{12} = -\Gamma_{23} \tag{54a}$$

and we know

$$\Gamma_{12} = -\Gamma_{21} \tag{54b}$$

$$T_{21} = 1 + \Gamma_{12} \tag{54c}$$

$$T_{12} = 1 - \Gamma_{12} \tag{54d}$$

Substituting Eq. 14(a) to Eq. 14(d) into Eq. (13), we can obtain

$$\Gamma_{in} = \frac{(1 - \exp(-2j\beta l))\Gamma_{12}}{1 - \Gamma_{12}^2 \exp(-2j\beta l)} \tag{55}$$

Similarly, we can obtain the total transmission coefficient

$$T_{out} = T_{21}(1+\Gamma_{23})\exp(-j\beta l) + T_{21}(1+\Gamma_{23})\exp(-3j\beta l)(\Gamma_{12}\Gamma_{23}) + \ldots \tag{56}$$

Now the common ratio is $\exp(-2j\beta l)\Gamma_{12}\Gamma_{23}$, so by applying Eq. (52), we can get:

$$T_{out} = \frac{T_{21}(1+\Gamma_{23})\exp(-j\beta l)}{1 - \exp(-2j\beta l)(\Gamma_{12}\Gamma_{23})} \tag{57}$$

Again substituting Eq. 54(a) to Eq. 54(d) into Eq. (57), resulting in

$$T_{out} = \frac{(1-\Gamma_{12}^2)\exp(-j\beta l)}{1 - \exp(-2j\beta l)\Gamma_{12}^2} \tag{58}$$

Eliminating the exponential terms in Eq. (55) and Eq. (58), we can get

$$\Gamma_{12}^2 S_{11} - \Gamma_{12}(S_{11}^2 - S_{21}^2 + 1) + S_{11} = 0 \tag{59}$$

Also we can present Γ_{12} in terms of the intrinsic impedance:

$$\Gamma_{12} = \frac{\eta_2 - \eta_1}{\eta_2 + \eta_1} = \frac{\eta_r - 1}{\eta_r + 1} \quad \text{, where} \quad \eta_r = \sqrt{\frac{\mu_r}{\varepsilon_r}} \tag{60}$$

Substituting Eq. (60) into Eq. (59) results in

$$\eta_r = \pm\sqrt{\frac{(1+S_{11})^2 - S_{21}^2}{(1-S_{11})^2 - S_{21}^2}} \tag{61}$$

Similarly, we can eliminate the Γ_{12} in Eq. (55) and Eq. (58), which is

$$\exp(-j\beta l) = \exp(-jk_0 nl) = \frac{S_{21}}{1 - S_{11}\Gamma} \tag{62}$$

or

$$\exp(-j\beta l) = \frac{-(S_{11}^2 - S_{21}^2 - 1) \pm \sqrt{(S_{11}^2 - S_{21}^2 - 1)^2 - 4S_{21}^2}}{2S_{21}} \tag{63}$$

where k_0 is the free space wavenumber, and n is the refractive index. Also assuming exp(-jβl)=z, we can present refractive index as:

$$n = \frac{1}{k_0 l}\{[\ln(z)'' + 2m\pi] - j[\ln(z)]'\} \tag{64}$$

where m is an integer.

Here we should set the conditions for this method. Since we are considering passive structures, it is subject to the criterion dictating proper choices of the signs of η and n, which are:

$$\eta' \geq 0 \quad \text{and} \quad n'' \geq 0 \tag{65}$$

At last, we can retrieve the effective relative permittivity and permeability easily through Eq. (61) and Eq. (64)

$$\varepsilon_r = \frac{n}{\eta}, \mu_r = n\eta \tag{66}$$

The wavenumbers can be obtained from Eq. (65)

$$k = \omega\sqrt{\varepsilon_0 \varepsilon_r \mu_0 \mu_r} \tag{67}$$

It should be noticed that the retrieved effective relative permittivity and permeability will have variation with the frequency since the input data of scattering parameters are functions of the frequency. Also it is important to know that they are not the only solutions. The reason is that we can notice in Eq. (64), as different integer m is chosen, different n will be obtained, yielding different results in Eq. (66). That is the reason we need to build the conditions of Eq. (65). To make this method reasonable, it is necessary to use another value of m manually if we find that η or n does not satisfy the conditions in Eq. (65).

4-3 Verification

In the beginning, the rationalities of the retrieved data in Eq. (67) will be examined. We construct a new homogeneous material whose effective permittivity and permeability are the data retrieved by the above mentioned method, and then inspecting the scattering parameters of the new material. Figure 30 shows the comparison between the corrugation and new material for the scattering parameters. The deep of S_{21} obtained by retrieving method is shallow, which is caused by the limit when setting a dispersive material in the full-wave simulators, but it is clear that the range of the stopband is similar, which means that characteristic of the new material can indeed be equivalent to the one of corrugation.

Two arbitrary cases will be proved, and the dimensions are as following: d = 8mm, d_z=1.8mm, g=1.6mm, and the relative permittivity are 10.2 and 6.15, respectively. Figures 31 show the scattering parameters for these two cases, and Figs. 32 are their corresponding dispersion diagrams in ACBC method and retrieving method. We can see that retrieving method matches to the ACBC method almost perfectly. By using this method, we can get not only just the scattering parameters, but also more information which is like phase velocity at measurement stage in the future.

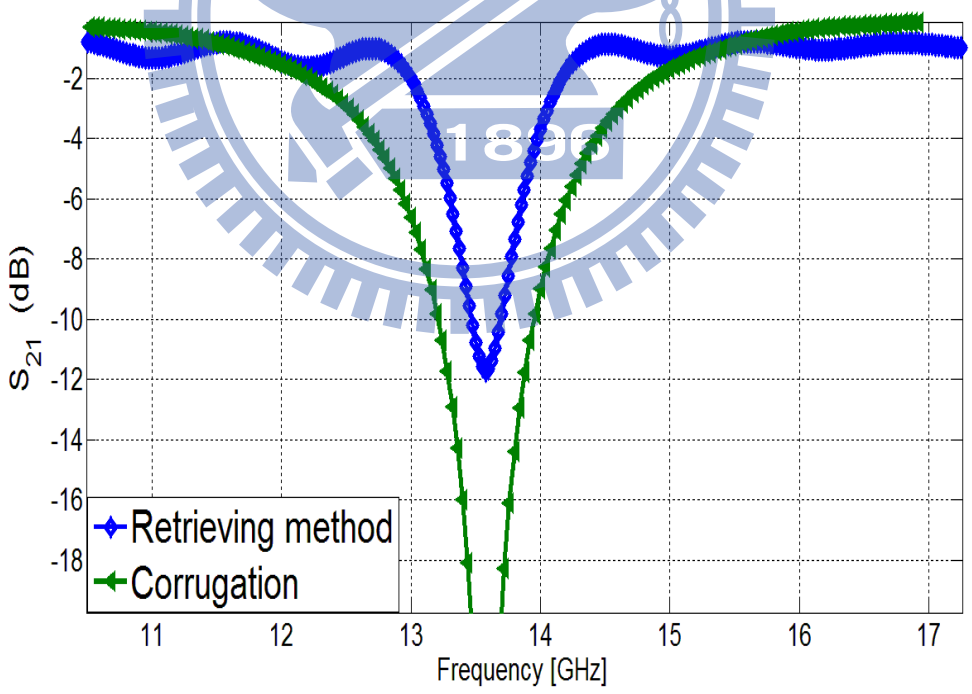

Figure 30: Comparison between the new material and the corrugation for the S_{21}.

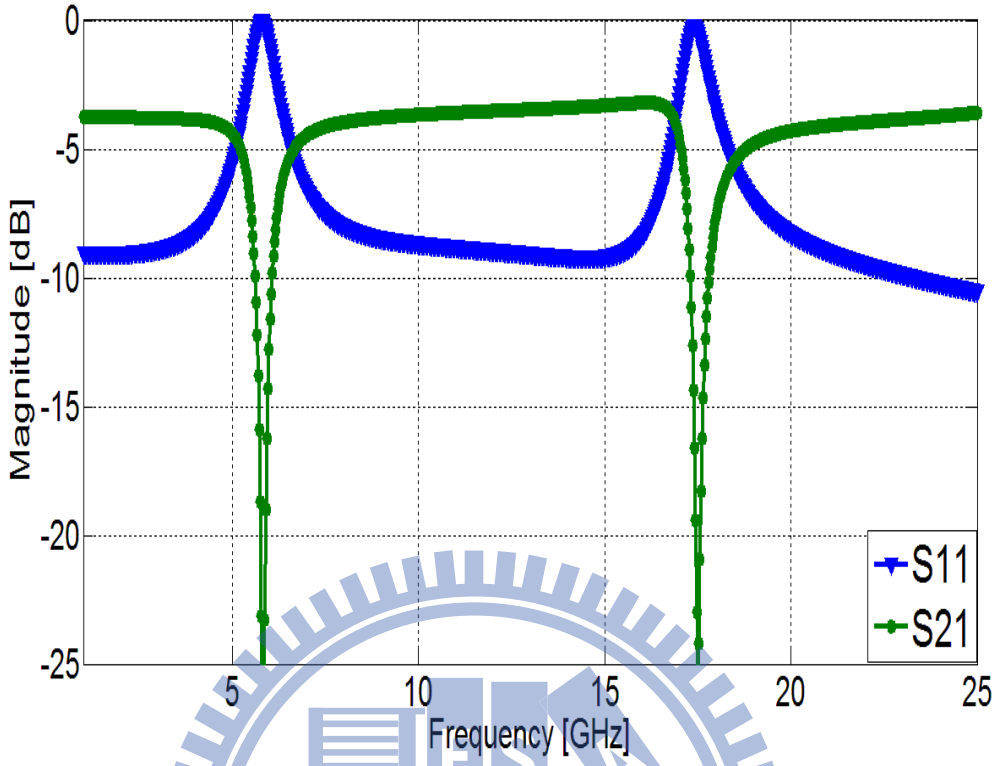

Figure31 (a): Scattering parameters for the relative permittivity of the grooves as 10.2.

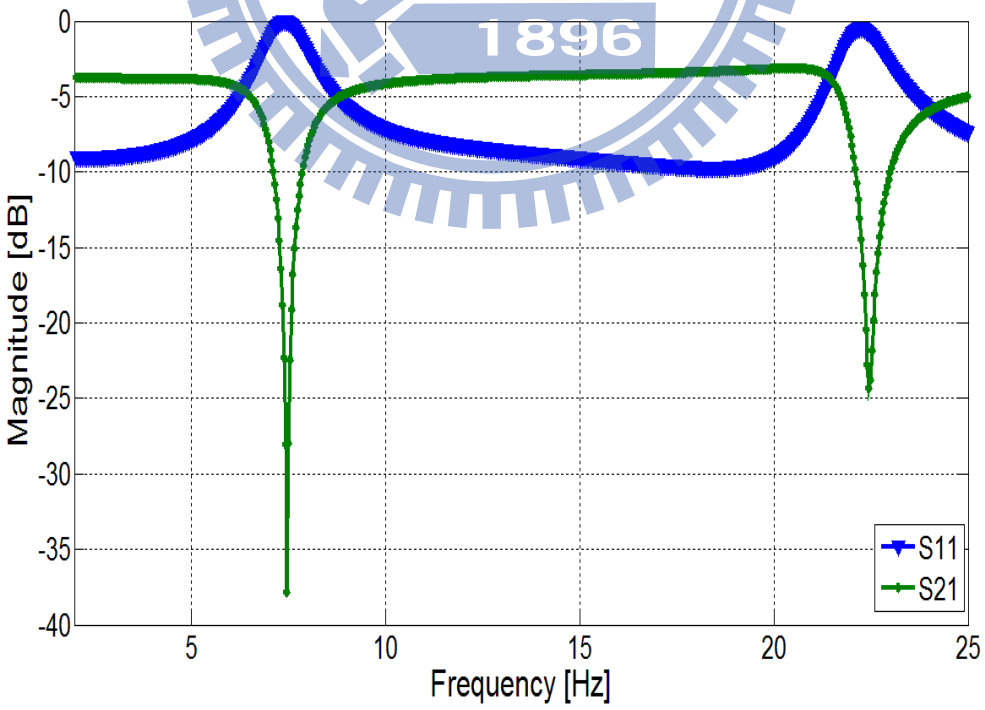

Figure 31 (b): Scattering parameters for the relative permittivity of the grooves as 6.15.

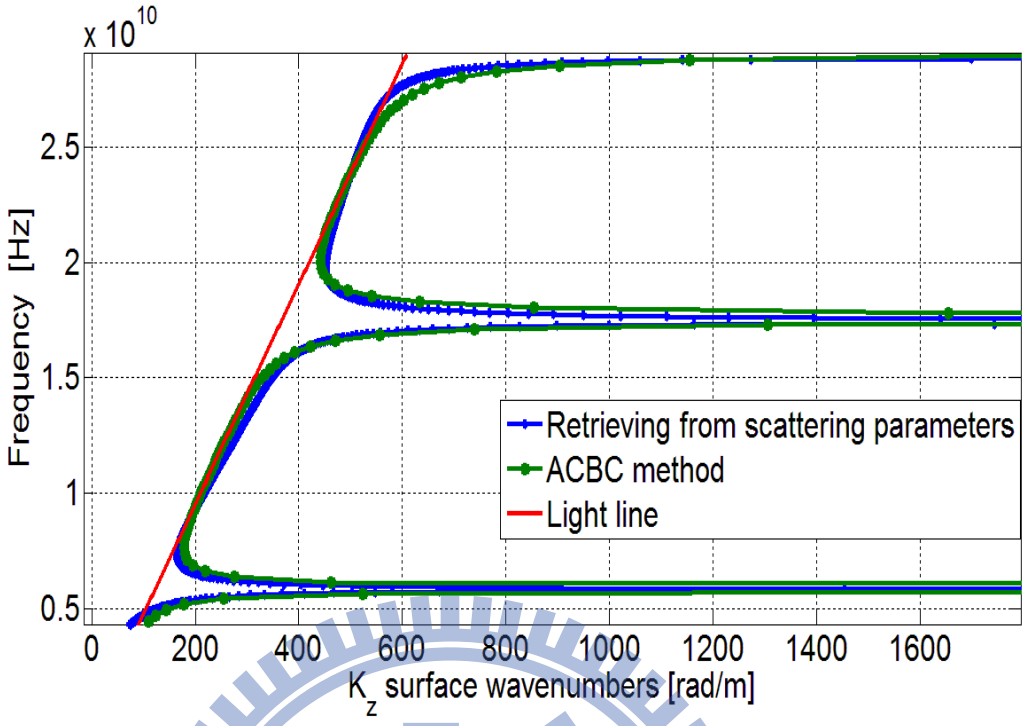

Figure 32(a): Comparison between the corrected ACBC method and retrieving method from scattering parameters as the relative permittivity is 10.2.

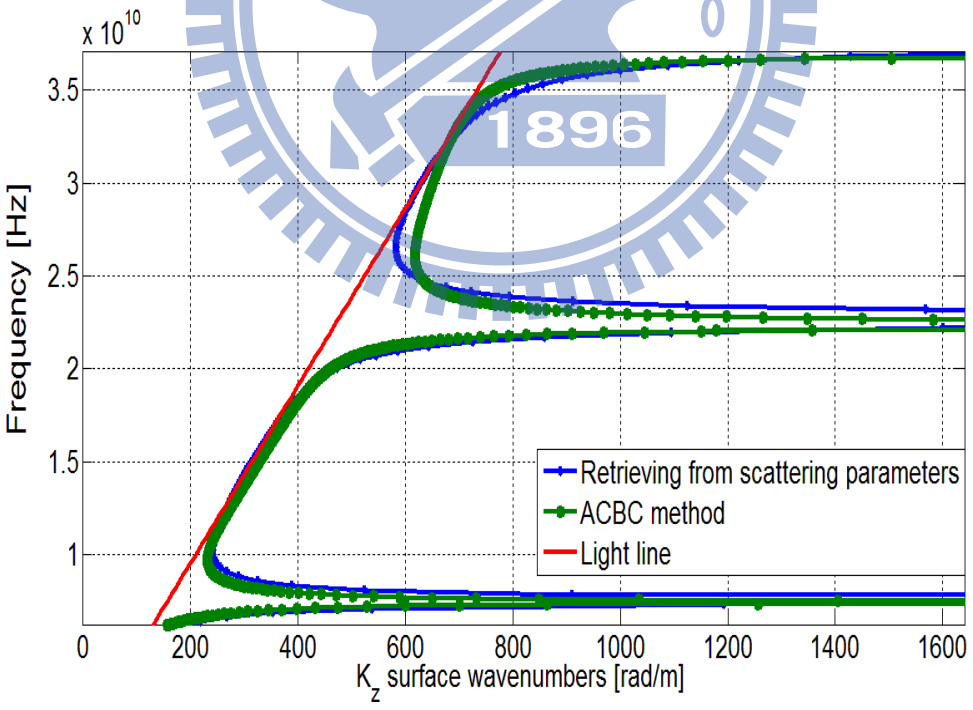

Figure 32(b): Comparison between the TRT method and retrieving method from scattering parameters as the relative permittivity is 6.15.

V. Conclusion

In this thesis, a new approximation to analyze slow waves on planar corrugated surfaces has been proposed. Based on the ACBC, we can derive the characteristic equation of the corrugation via applying the vector potential method. Also compared to the CST software and TRT, it is shown that for the ACBC method, its accuracy is as good as CST and the speed is as fast as TRT, i.e. extracts the advantages from both.

Meanwhile, a novel idea has also been proposed by applying the characteristic equation obtained by ACBC method, which is called sectorial bandgap. Indeed, for most of the periodic structures which are always designed for wider bandgap for any direction, there are potential applications that the bandgap may be needed just in some directions over a certain frequency range. For example, the corrugations may be used for controlling the direction of signal propagation in microwave circuits. Another potential application is the reduction of the cross polarization of some antennas. In Chapter III, we also present a kind of guideline to show how to design a sectorial bandgap corrugation, which cannot be done for other periodic structures without their own characteristic equations.

At last, the relationship of the scattering parameters and the wavenumbers is introduced. Due to the complex equivalent circuit of the corrugations, the use of ABCD matrix is not proper here. Instead, an interesting aspect based on [17] is shown, which is to take the corrugation as a new whole structure, and the last dispersion diagram transformed from scattering parameters are matched well to the ACBC method.

The work in this thesis is not the end but a pioneer, since we hope to reach the potential application we mentioned above in the future, and also we wish to provide a more accurate guideline to let the designers reach their standard.

Reference

[1] R. S. Elliott, "On the theory of corrugated plane surfaces," *IRE Trans. Antennas Propag.*, pp. 71-81, Apr 1954.

[2] R. W. Hougardy and R. C. Hansen, "Scanning surface wave antennas – oblique surface waves over a corrugated conductor," *IRE Trans. Antennas Propag.*, pp. 370-376, Oct 1958.

[3] P.-S. Kildal, "Definition of artificially soft and hard surfaces for electromagnetic waves," *Electronic Letters*, vol. 24, no. 3, pp. 168-170, Feb. 1988.

[4] P.-S. Kildal, "Artificially soft and hard surfaces in electromagnetics," *IEEE Transactions on Antennas & Propagation*, vol. 38, no. 10, pp. 1537-1544, Oct. 1990.

[5] J.A.Aas and P.-S. Kildal, "Reduction of forward scattering from struts in reflector antennas," *Proc. 18th European Microwave Conf.*, Stockholm, Sept. 1988, pp.494-499

[6] F. Yang and Y. Rahmat-Samii, "*Electromagnetic Band Gap Structures in Antenna Engineering*," Cambridge RF and Microwave Engineering Series, Cambridge Univ. Press, Nov 2008.

[7] F. Yang and Y. Rahmat-Samii, "A low-profile circularly polarized curl antenna over an electromagnetic bandgap (EBG) surface," *Microwave Optical Tech. Lett.*, vol.31, no. 4, 264-7, November 2001.

[8] A. R. Weily, L.Horvath, K. P. Esselle, B. C. Sanders, and T. S. Bird, "A planar resonator antenna based on a woodpile EBG material," *IEEE Transactions on Antennas & Propagation*, vol.53, no. 1, 216-23,2005.

[9] R. Coccioli, F.R. Yang, K.P. Ma, and T. Itoh, "Aperture-coupled patch antenna on UC-PBG substrates," *IEEE Trans. Microwave Theory Tech*, vol. 47, 2131-8, 1999.

[10] T. M. Uusitupa, "Usability studies on approximate corrugation models in scattering analysis," *IEEE Trans. Antennas Propag.*, vol. AP-54, no. 9, pp. 2486-2496, Sep 2006.

[11] H. A. Kalhor, "Approximate analysis of electromagnetic scattering from corrugating conducting surfaces by surface impedance modeling," *IEEE Trans. Antennas Propag.*, vol. AP-25, pp. 721-722, Sep 1977.

[12] P.- S. Kildal, A. Kishk, and Z. Sipus, "Asymptotic boundary conditions for strip-loaded and corrugated surfaces," *Microw. Opt. Technol. Lett.*, vol. 14, no. 2, pp. 99-101, Feb. 1997.

[13] D.Sievenpiper, L.Zhang, R. F. J. Broas, N.G. Alexopolus, and E. Yablonovitch, "High-impedance electromagnetic surfaces with a forbidden frequency band," *IEEE Trans. Microwave Theory Tech.*, vol.47, 2059-74,1999.

[14] Wei-Zhang, Chang-Hong Liang, Tong-Hao Ding, and Bian Wu, "A novel broadband EBG using multi-via cascaded mushroom-like structure," ***2009 Asia-Pacific Microwave Conference,*** Singapore , Dec.2009.

[15] C. H. Walter, *Traveling Wave Antennas*, Chapter 6, pp. 259-260, Peninsular Publishing, 1965.

[16] D. M. Pozar, *Microwave Engineering*, 2nd ed. New York: Wiley, 1998.

[17] A. M. NICOLSON and G.F. Ross, "Measurement of the Intrinsic Properties of Materials by Time-Domain Techniques," *IEEE TRANSSACTIONS ON INSTRUMENTATION AND MEASUREMENT*, vol. IM-19, No. 4. Nov. 1970.